Evolution of damage in grade 2 and grade 4 titanium sheets during cyclic bending under tension and simple tension

Nicholas Pitkin[a], Philip Noell[b], David T. Fullwood[c] and Marko Knezevic[a,*]

[a] Department of Mechanical Engineering, University of New Hampshire, Durham, NH 03824, USA.
[b] Materials, Physical, and Chemical Sciences Center, Sandia National Laboratories, Albuquerque, NM 87185-0889, USA.
[c] Department of Mechanical Engineering, Brigham Young University, Provo, UT 84602, USA.

[*] Corresponding author e-*mail address*: marko.knezevic@unh.edu (M. Knezevic).

Abstract

This paper describes a study into damage evolution, in the form of voids, in two different commercially pure titanium (CP-Ti) alloys subjected to cyclic bending under tension (CBT) and uniaxial tension (simple tension, ST). X-ray computed tomography (XCT) was used to observe the voids that developed in Grade 2 CP-Ti at various levels of deformation in both processes. The results were compared to those of our previous study on Grade 4 CP-Ti, to investigate the role of damage accumulation in formability of metal sheets achieved through CBT. The investigation showed that much greater elongations, and local strains were achieved by Grade 2 CP-Ti, when compared to Grade 4 CP-Ti, and this coincided with slower damage accumulation. In CBT, the elongation to failure (ETF) of Grade 2 and Grade 4 CP-Ti were 4.4x and 2.5x greater than in ST, respectively. Longitudinal strains in the bulk and in the localized regions of the Grade 2 and Grade 4 CP-Ti in CBT were significantly larger than the highest strains in the necked regions during ST. The greater strains in Grade 2 CP-Ti were accompanied by slower void nucleation and growth than in Grade 4 CP-Ti. When compared at similar levels of strain, the number of voids observed was 9.6x higher in Grade 4 than in Grade 2 CP-Ti, and the average void radius was also 1.4x higher in Grade 4 CP-Ti. Additionally, the average void size increased significantly throughout CBT in Grade 4 CP-Ti, while moderately in Grade 2 CP-Ti. In both alloys, however, it was shown that CBT does not delay damage accumulation, when compared with ST, but allows for further plastic deformation despite it. The results provide insights into the role of damage accumulation on the ability of CBT to delay failure in CP-Ti sheets.

Keywords: Commercially pure titanium; Voids; Damage; Microstructures; Cyclic-bending-under-tension; Simple tension.

1. Introduction

Recently, various industries have steered toward the adoption of lightweight and high strength materials for automobiles [1-3], aircraft [4-7] and watercraft [8], in an effort to decrease fuel consumption (and subsequent emissions and operating costs), while increasing performance. Similarly, energy production can benefit from the use of lightweight components, e.g. windmill turbines [9], steam turbines [10] and hydroelectric water wheels [11]. Popular materials with high strength-to-weight ratios include fiber or particle reinforced polymers [12-18], as well as lightweight metals, such as aluminum, magnesium and titanium [19-23]. Titanium is of particular interest due to its corrosion resistance and biocompatibility [24-26]. However, difficulties arise in forming lightweight metals with hexagonal close-packed (HCP) structure, like magnesium and titanium, due to their distinctive mechanical properties, such as high anisotropy/asymmetry [27-30] and low ductility [31]. These properties are due, in large part, to the limited number of active slip systems in HCP materials, requiring the activation of twin systems to achieve the necessary number of degrees of freedom to accommodate plastic strains [32-34]. Though improvements in formability can be found through various processes such as single point incremental forming [35] and electropulsing-assisted incremental forming [36], metal sheet-forming often requires the material to be heated to high temperatures in order to attain desired results [37, 38]. Hot forming processes enable forming of complex shapes from metal sheets, but the energy input required to reach and sustain high temperatures can be very costly and have negative consequences for the environment. This provides impetus for investigating novel room-temperature sheet-forming methods for hard-to-form metals.

One such novel sheet-forming method is cyclic-bending-under-tension (CBT) [39]. The CBT process presented in this study improves the elongation to failure (ETF) of metallic sheets by reciprocally traversing a thin sheet through a set of three rollers while a constant, nominal tensile displacement rate, v, is applied. The three rollers impart bending to the sheet, which is determined by the roller spacing, roller diameter and bend depth, δ, of the central roller. This CBT configuration is shown in **Fig. 1**. To better understand the origins of varying improvements in elongation to failure (ETF) of different materials in CBT, two commercially pure titanium (CP-Ti) alloys were investigated in terms of mechanical response and damage evolution, in the form of microvoids, after incremental deformation in CBT and simple tension (ST). Additionally, the observations of void-based damage provide insights into the final structural state of the materials after being processed by CBT.

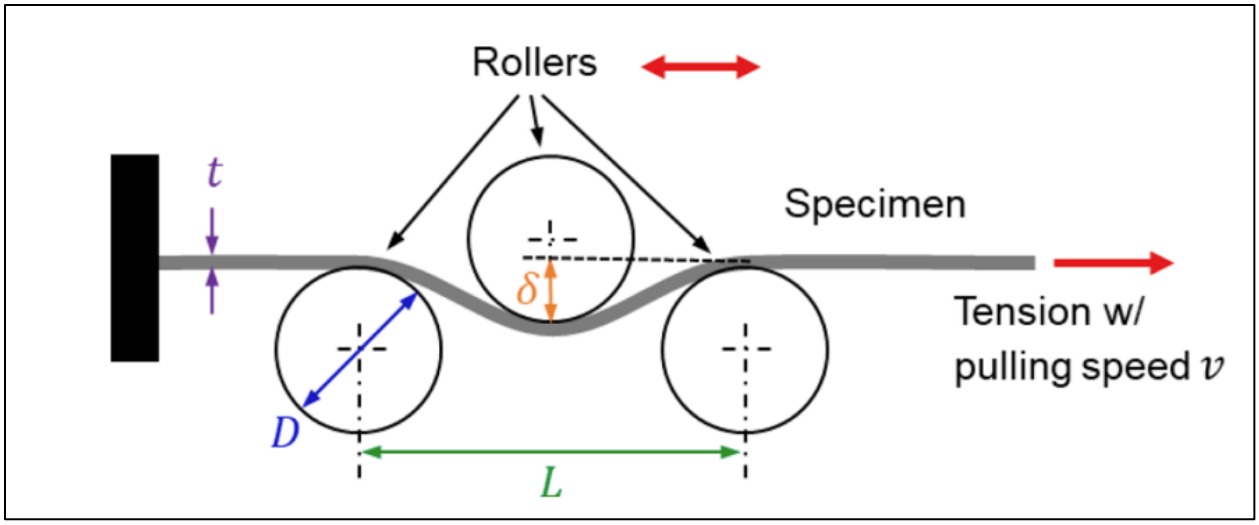

Fig. 1: Schematic of the CBT process showing various parameters. The span between the lower rollers, *L,* is fixed at 54mm, and the diameter of the rollers, *D,* is fixed at 25.4mm.

The key mechanism of the CBT process, that allows sheets undergoing CBT to achieve much greater elongations than in ST, is that it delays localization by incrementally depleting the ductility of sheets [40-42]. As the flow stress in the sheet is highest near to contact points with the rollers, where a combination of bending and tension occurs (**Fig. 1**), the bulk of plastic deformation is limited to the portions of the sheet close to these contact points [43]. The changing position of the rollers, relative to the sheet, results in incremental elongation. The increased ETF of materials in CBT over ST is largely attributed to its incremental nature, with effects relating to microstructure, stress state or reversal of dislocations, for example, being believed to play a lesser role [44]. However, Sharma et al. [45] found that the incremental nature of CBT accounted for only half of the increase in elongation over ST of AHSS TRIP steels, as local strains in CBT reached values about twice as high as in ST. By contrasting the damage evolution of two materials in CBT and ST, insights into the mechanisms behind the increased elongation to failure afforded by CBT, and why they may differ between materials, could be obtained. Moreover, the compression applied by the rollers and alternating compression owing to the bending in the localized regions subjected to plastic strain along with simultaneous relaxation in the rest of the sheet are secondary mechanisms.

Additionally, understanding and predicting the failure process benefits from modeling damage accumulation and ductile failure processes. Previous developments in this area include works by Tvergaard and Needleman [46, 47] and implementations of the Gurson-Tvergaard-Needleman (GTN) damage models [48-50]. By investigating damage accumulation in CBT, data is provided that can inform future damage models specifically tailored for the CBT process. These would be valuable tools to further understand the greater elongations achieved in CBT over ST, and design manufacturing processes inspired by the CBT process.

The two CP-Ti alloys in the current investigation, Grade 2 and Grade 4 CP-Ti, were chosen because they are suitable candidates for improved formability via incremental forming such as under CBT. As both alloys fail after profuse necking in monotonic tensile testing, much ductility is left to be depleted throughout the rest of the gauge section. During CBT, this remaining ductility is depleted evenly across the sample by the moving rollers. Improvements in the formability of Grade 4 CP-Ti have been demonstrated in previous studies [40, 51-53], while the

current study is the first to investigate Grade 2 CP-Ti in CBT. Differing concentrations of trace elements in the two alloys constitute the major difference between them. Of these trace elements, oxygen is notable, as its addition, even in small amounts, to titanium has been shown to substantially decrease ductility and increase strength [54-58].

Tensile failure of ductile materials, such as CP-Ti, is typically caused by microvoids that nucleate, grow and coalesce as the material is deformed. Mechanisms by which voids form include vacancy condensation [59, 60] and strain incompatibilities between impurities and the surrounding metallic matrix, resulting in debonding [61-63] and/or impurity cracking [63, 64]. Common sites of void nucleation in metallic materials include grain boundaries [65-67], twin boundaries [65, 66, 68], phase boundaries [69, 70] and deformation-induced cell walls and cell-block boundaries [71, 72], among others. Voids facilitate failure in ductile metals when the material between them (intervoid ligaments) neck or shear, causing the voids to coalesce until the material ruptures entirely [73, 74], leaving behind the characteristic dimpled fracture surface [75, 76]. The process of ductile failure is dependent on the material and loading conditions to which it is subjected [77-80]. For example, Horstemeyer and Gokhale [78] compared the void content of 4340 steel, silicon-aluminum and HY180 steel from studies by Cox and Low [81], Fisher and Gurland [82] and Maloney and Garrison [83], respectively. This data showed that, when compared at similar levels of strain, less ductile materials accumulated a greater number density of voids. Additionally, void nucleation increased when the material had a lower fracture toughness and contained bigger inclusions. Samei et al. [80] investigated the effect of strain paths on void accumulation in dual-phase steel sheets. At similar strains, the greatest number of voids were shown to accumulate in plane-strain testing, followed by biaxial and uniaxial tension, respectively. A similar study by Pathak et al. [79] showed the dependence of void accumulation on stress state by testing CP800 and DP780 steels in uniaxial tensions, biaxial tension, plane strain and shear. Additionally, Horstemeyer et al. [77] observed damage accumulation in Al-Si-Mg under tension, compression and torsion. It was shown that void nucleation was similar in tension and torsion but was greatly diminished in compression. Several studies have also reported on the effects of stress triaxiality on void nucleation and growth, often using notched tensile specimens. These have shown that void nucleation strain decreases with an increase in stress triaxiality [62, 79, 84-86].

In summary, many efforts have been put forth to investigate the damage accumulation of various materials under different loading conditions. However, only one publication has reported on void-based damage evolution in CBT [51]. By comparing the damage evolution of two materials in CBT and ST, the role of damage accumulation in the ability of CBT to achieve greater ductility, over ST, can be better understood. Additionally, the data obtained can be used into future plasticity-damage modeling efforts of the CBT process. The effects of small changes in alloy composition on the damage accumulation in titanium alloys are also highlighted.

2. Experimental procedures

2.1 Preparation of test sheets

CBT strips were cut from nominally 1mm thick sheets of Grade 2 and Grade 4 commercially pure titanium (CP-Ti) using a waterjet. The composition of each alloy is shown in **Table 1**. Each strip was 240mm in length and the width of each sheet was 11.7mm. The edges of the strips were hand-ground using abrasive paper until all had an acceptably smooth surface finish. The five regions of the CBT strip are shown in **Fig. 2** (two 1×, two 2× and one 3× regions), and these are

defined by the number of rollers that move over the region in a single pass. The 3× region is of greatest interest, as the bulk of elongation occurs in this portion of the strip. Because of this, the length of the strip was chosen such that initial length of the 3× region was sufficient (in this case, the initial length of the 3× was 50mm). Additionally, the use of strips, as opposed to dog-bones, is possible in CBT, since the strips reliably break near the interface of the 2× and 3× regions; there is no need to create a thinner gauge length to ensure failure away from the grips. The modified ASTM-E8 dog-bone specimens used in tensile tests (simple tension, ST) were also cut from the 1mm thick sheets and the edges were hand-ground to a smooth surface finish. The gauge length of the ST dog-bone was 175mm, the initial distance that the rollers traverse in a single pass in CBT, when measured at the edge of the outermost roller at each end of the pass. The gauge length of the ST specimen is selected equal to the initial length that the rollers act upon in CBT. However, it should be noted that the gauge section of 175 mm stretched in tension will be compared with the gauge section of essentially 50 mm (the 3× region) stretched in CBT. While the 1× and 2× regions also are strained but much less compared to the 3× region. Therefore, the displacements that will be presented underrepresent the increased displacement in the CBT tests compared to that of the tension tests. Nevertheless, the dimensions are consistent with the prior work [51].

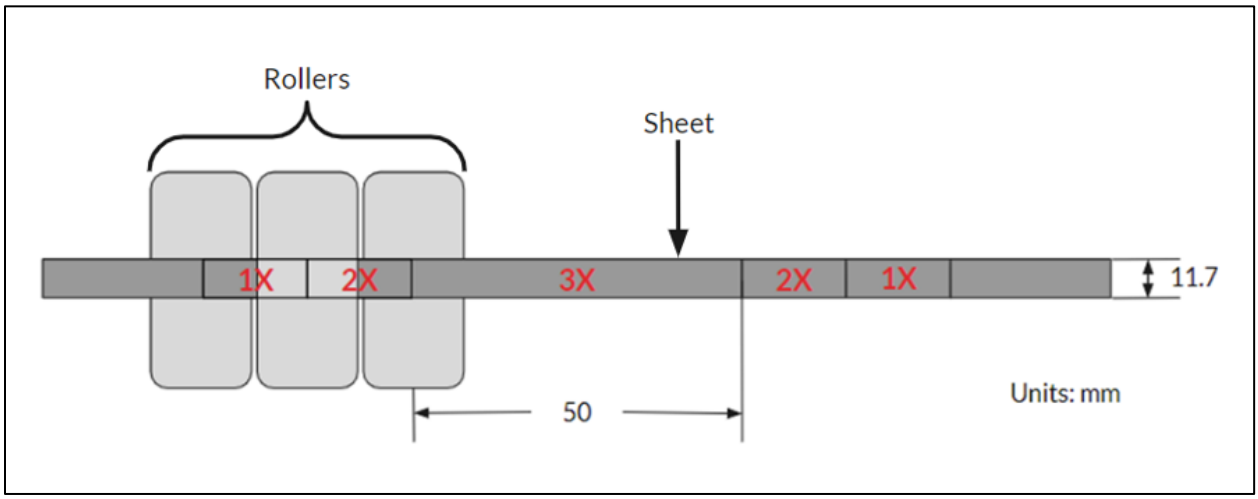

Fig. 2: Diagram of initial CBT sheet used in this study with 1×, 2× and 3× regions indicated. All sheets had an initial thickness of 1mm. Note that, given a roller diameter of 25mm, the distance from the left most roller at the left end of a pass to the right most roller at the right end of a pass is 175mm.

Table 1: Chemical compositions of Grade 2 and Grade 4 CP-Ti sheets used in the study.

	Carbon (%)	Iron (%)	Hydrogen (%)	Nitrogen (%)	Oxygen (%)	Titanium (%)
Grade 2 CP-Ti	0.004	0.08	N/A	0.01	0.09	Balance
Grade 4 CP-Ti	0.005	0.19	0.0006	0.004	0.25	Balance

2.2 CBT and ST testing with digital image correlation

Both CBT and ST tests were performed with the purpose-built CBT machine at the University of New Hampshire. Details of this apparatus can be found in Roemer et al. [41]. The two variable parameters for these CBT tests are bend depth (δ in **Fig. 1**) and the tensile displacement rate (pull speed, *v,* in **Fig. 1**), as explained above. The roller spacing, roller diameter and carriage speed (66 mm/s is the speed at which the sheet traverses through the rollers) are fixed for all tests with this machine. The combination of bend depth and pull speed that results in the greatest ETF during CBT are considered the optimal parameters for a given material. For the strips of Grade 2 CP-Ti, bend depth and pull speed optimization tests were performed, and it was determined that the optimal bend depth and pull speed were 5.5mm and 1.55mm/s, respectively. In a previous work [87], the optimal bend depth and pull speed for Grade 4 CP-Ti were found to be 3.5mm and 1.3mm/s, respectively. All CBT tests conducted in this study used the optimal parameters for each alloy, and all strips were loaded in the rolling direction (RD).

For tests with the CBT machine, displacement was measured by the Balluff Micropulse position sensor attached to the hydraulic actuator of the machine. Digital image correlation (DIC) was used to generate strain maps in regions of interest throughout the CBT tests. For this, CP-Ti sheets were painted with Rust-Oleum® high-heat spray paint, with white paint being used as the base and black paint being used for the speckle pattern. High-contrast images were taken at two images per second with a Point Grey GRAS-20S4M-C camera and Schneider Xenoplan 1.4-17mm with a resolution of 2MP (resolution of 0.044 mm/pix). Correlated Solutions® VIC-Snap software was used to capture the images during the test. The camera was positioned above the 2×/3× region on the side of the fixed grip, such that this region would not move out of view of the camera. Analysis was performed in VIC-2D using a subset-based method, which is capable of making strain calculations at large displacements. For the analysis, a subset of 19 and step size of 4 were used. Due to visual interference from the rollers during CBT, analysis was only performed on images in which the rollers were out of view of the camera.

All ST tests in this study were performed using a nominal engineering strain rate of $0.001s^{-1}$ in the RD direction at room temperature. This strain rate was chosen to test the mechanical properties of the materials under a quasi-static condition. It should be noted, however, that the nominal engineering strain rate during CBT is not constant but averages to about $0.005s^{-1}$. The ST tests were conducted using the purpose-built CBT machine, and results were validated by performing tests on an MTS servo-hydraulic machine. For tensile tests performed with the CBT machine, displacement was measured by the position sensor attached to the hydraulic actuator of the machine, and then converted to engineering strain. DIC was used to measure strain during tensile tests. A comparison of engineering stress-strain curves from representative monotonic tensile tests performed with both methods is shown in **Fig. 3**. Properties such as UTS and strain at failure were similar for tests performed on both machines. Slight differences in the curves near failure are apparent, but the overall consistency of tests using both machines leads to the conclusion that tensile tests using the CBT machine are valid. It should be noted that, of four tensile tests of Grade 2 CP-Ti, the standard deviation in failure strain was 0.00466, and the standard deviation in UTS was 5.16MPa.

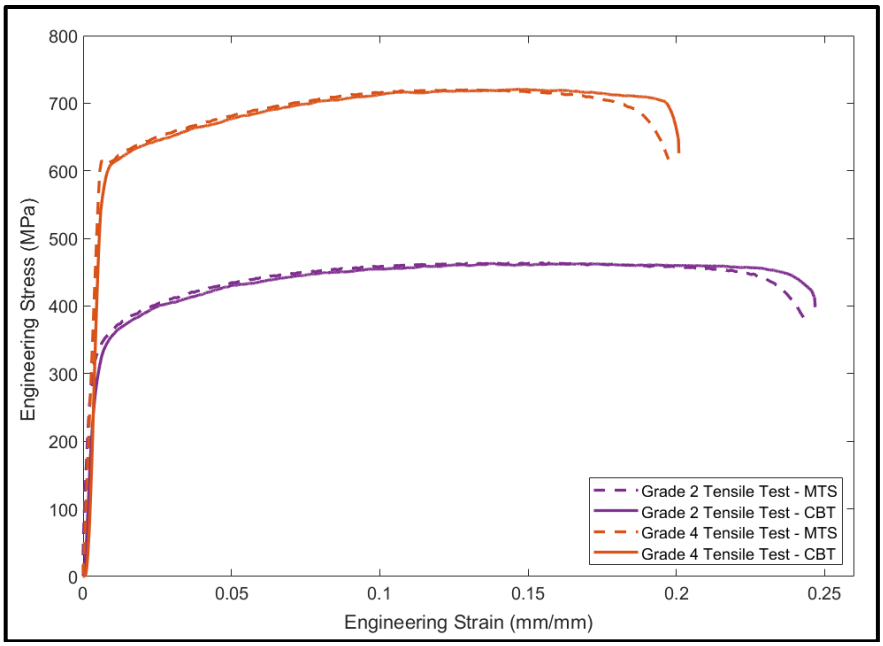

Fig. 3: Engineering stress-strain curves for Grade 2 and Grade 4 CP-Ti sheets measured in ST using the purpose-built CBT machine and MTS.

2.3 Damage observation through X-ray computed tomography

In our previous work [51], sub-specimens were cut from deformed Grade 4 CP-Ti strips after CBT and deformed dogbone specimens after ST. Sub-specimens of about 1mm in the RD direction were cut from the sheets, as shown in **Fig. 4.** The thickness and width of the sub-specimens spanned the entire thickness and width of the larger sheet at the location that the sub-specimens were cut from. In the previous work, sub-specimens were cut from the mid-length 3× region (**Fig. 2**) after 9, 11 and 12 CBT cycles and at the 2×/3× interface (the necking region) after 12 CBT cycles. Sub-specimens were cut from the mid-length 3× and the 2×/3× to understand the damage accumulation in the region where the bulk of elongation occurs and to observe the extent of damage accumulation that precedes failure in the localized region. Sub-specimens were also cut from the most severely necked region of tensile dogbones after being pulled to engineering strains of 0.176, 0.189 and 0.194, termed the Grade 4 G4-0.176, G4-0.189 and G4-0.194 specimens, respectively.

In the present study, Grade 2 CP-Ti sub-specimens were cut from the mid-length 3× region and 2×/3× interface (the necking region) of strips after 14, 17 and 18 CBT cycles at the optimal parameters determined for Grade 2 CP-Ti. Sub-specimens were also cut from tensile dogbones after being pulled to strains of 0.205, 0.237 and 0.243, termed the Grade 2 G2-0.205, G2-0.237 and G2-0.243 specimens, respectively. The deformation levels were chosen such that each Grade 2 CP-Ti sample approximately matched a Grade 4 CP-Ti sample, in terms of the deformation level as a percentage of the elongation-to-failure (%ETF). The %ETF was calculated by dividing the displacement of a given sheet by the displacement at which failure occurred in a reference test for that material.

Using a Zeiss Xradia Versa 620, X-ray tomography was conducted with all Grade 2 and Grade 4 CP-Ti specimens. A beam voltage of 70kV and power of 8.5W was used during each of the scans. Using a binning of 1x1, a voxel size of approximately 3.1µm was achieved, with 1601 projections (radiographs) per 360^{o} rotation being taken. Five reference scans, each with ten

separate exposures without the sample, were taken to use for background subtraction and normalization of the tomograms. This was done at an interval of 350 projections. All scans were reconstructed in Zeiss XMReconstructor. This software uses a standard filtered back-projection algorithm. The XCT scans were analyzed in ORS Dragonfly. ORS Dragonfly's machine-learning segmentation feature was used to separate each of the scans into the airspace around the specimen, the specimen itself and the voids within the specimen. Between five and ten slices were used to train U-net and Random forest algorithms to segment the models into the three regions of interest (ROIs). Although the voxel size of the XCT scans suggests a spherical void of 3.1µm can be observed, a threshold for minimum void dimensions was imposed to ensure that noise in the images would not be mistakenly labeled as voids. For a void to be considered resolvable, it had to be about two voxels in length in every dimension (i.e. be at least 6.2µm in length, width and thickness). Voids below this threshold were discarded prior to any analysis. As such, all analyses of void volume density are lower-bound. Segmentation results were manually reviewed to ensure accuracy. All data from segmentation was processed in MATLAB.

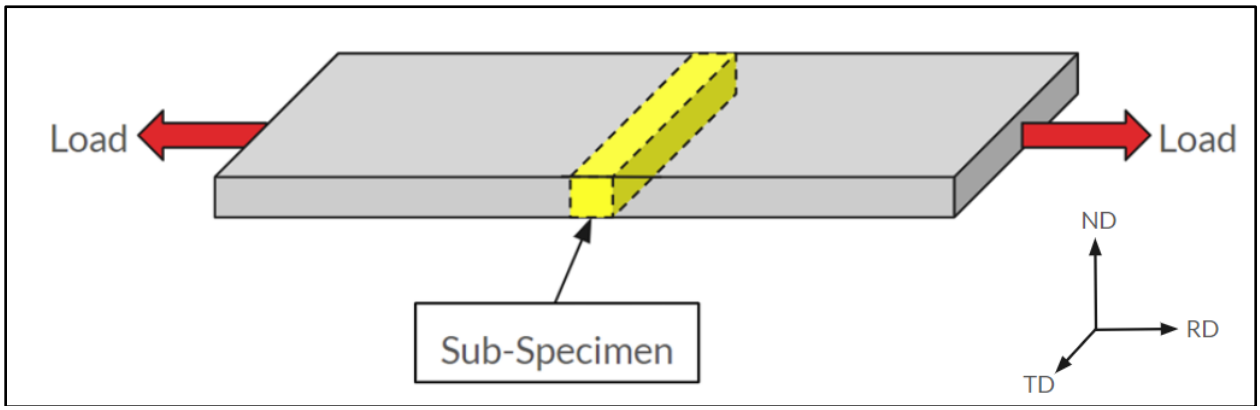

Fig. 4: Schematic showing sub-specimens cut from CBT and ST specimens.

2.4 Electron Backscatter Diffraction

To study the microstructural evolution of Grade 2 and Grade 4 CP-Ti, electron backscatter diffraction (EBSD) was performed. Careful grinding and polishing of the samples was done before EBSD was performed. For this, specimens were placed on an automated grinder with sequentially finer silicon-carbide papers of 320 to 1200-grit. For Grade 2 CP-Ti, specimens were polished on an automated lapping polisher with 1µm diamond suspension at 150RPM with a force of 5lbs/sample for ten minutes. For a final polish, a solution of four parts 0.05µm colloidal silica-ethylene glycol suspension to one part hydrogen peroxide (30%) was used in a vibratory polisher at 60Hz for 12 hours. The Grade 4 CP-Ti specimens were polished with 9µm diamond suspension at 150RPM with a force of 6lbs/sample for fifteen minutes. The final polish used the same suspension as Grade 2 CP-Ti on an automated lapping polisher at 100RPM with a force of 5lbs/sample for fifteen minutes.

A Tescan Lyra3 (Ga) field emission SEM was used with an EDAX Pegasus system (Octane Plus SDD detector and Hikari High Speed Camera) to perform EBSD. A working distance of 9mm was used for all scans. Scans were collected using EDAX APEX software with a step size of 0.1µm for higher-resolution scans and 0.5µm for lower-resolution scans. Post-processing was performed in TSL OIM Analysis 8 software. Confidence index (CI) correlation was performed,

where all points with a CI of less than 0.1 were replaced with neighboring points whose CI was greater than 0.1. Grain dilation, where points with a low CI are incorporated into the grain with the largest number of surrounding points, was used with a minimum grain size of five points.

3. Results

3.1 Mechanical response in ST and CBT

Testing of the Grade 2 and Grade 4 CP-Ti strips in CBT showed remarkable differences, especially when compared to their behavior in ST. During monotonic tensile testing, Grade 4 CP-Ti sheets reached an engineering strain of about 0.198 (or 34.7mm ETF), while the Grade 2 CP-Ti sheets reached a strain of about 0.246 (or 43.1mm ETF). This is a 1.24x increase in failure strain from Grade 4 to Grade 2 CP-Ti in ST. The ETF in CBT increased by 2.30x from Grade 2 to Grade 4 CP-Ti, with Grade 4 CP-Ti having an ETF of 82.3mm and Grade 2 CP-Ti having an ETF of 189.1mm. The ratio of ETF in CBT to ETF in ST is 2.37 for Grade 4 CP-Ti and 4.39 for Grade 2 CP-Ti. Results for CBT and ST testing of Grade 2 and Grade 4 CP-Ti are shown in **Fig. 5**. The contrast between Grade 2 CP-Ti sheets post-ST and post-CBT can be seen in the photograph of **Fig. 6**. An equivalent plot to **Fig. 6** for Grade 4 CP-Ti can be seen in [51].

The ultimate tensile strength (UTS) of the Grade 2 and Grade 4 CP-Ti was 462.99MPa and 726.76MPa, respectively, as measured during monotonic tensile testing on the CBT machine. Due to the bending stress imparted by the rollers during CBT, there was a marked reduction in the maximum engineering stress measured during CBT for both materials, with the maximum engineering stress of the Grade 2 CP-Ti CBT sheet being 319.48MPa, and 578.01MPa for the Grade 4 CP-Ti sheet; i.e. the maximum tensile load experienced by the sheet in CBT was 0.69x and 0.80x the maximum load in ST, for the Grade 2 and Grade 4 CP-Ti, respectively. The greater decrease in maximum load exhibited by Grade 2 CP-Ti is due to the higher bend depth applied during CBT.

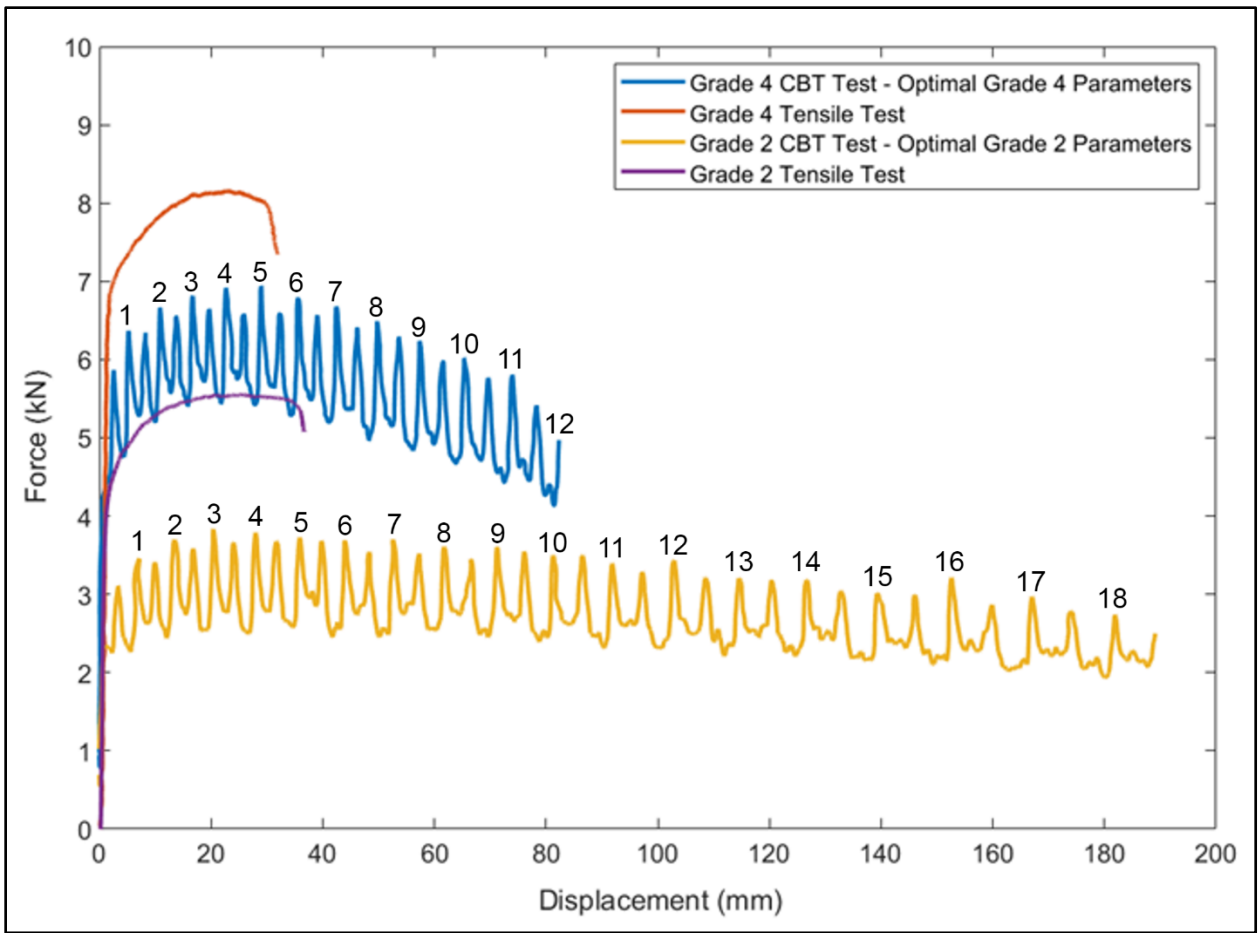

Fig. 5: Force-displacement plots for Grade 2 and Grade 4 CP-Ti in CBT and ST, with numbers indicating the end of each cycle.

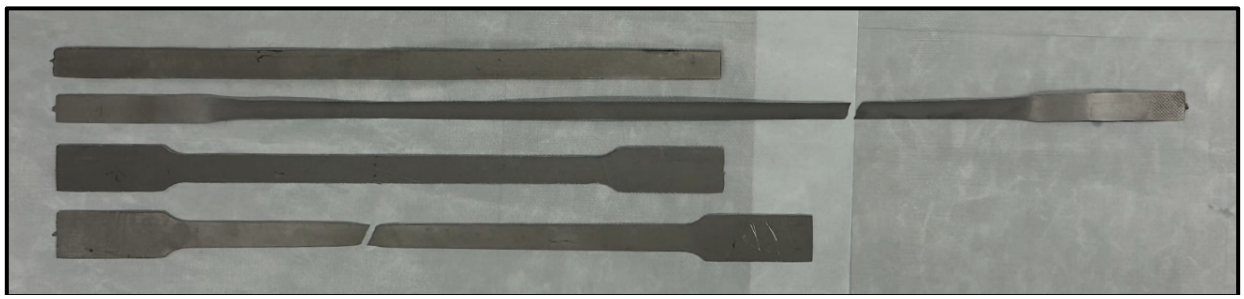

Fig. 6: Comparison of (top to bottom) initial CBT strip specimen, post-mortem CBT strip specimen, initial tensile dog-bone and post-mortem tensile dog-bone of Grade 2 CP-Ti.

Strain maps showing longitudinal (major) strain measured during ST and CBT testing of Grade 2 CP-Ti are shown in **Fig. 7a** and **Fig. 7b**, respectively. Each image shows the approximate strain on the surface of the sheet when each of the sub-specimens were extracted. Grade 2 CP-Ti exhibited uniform elongation during the ST test to an engineering strain of 0.205. Localization is evident at an engineering strain of 0.237, and very profuse necking occurred by an engineering strain of 0.243. The maximum longitudinal strain in the necked region of the ST

specimens rapidly increased from 0.347 to 0.456, at engineering strains of 0.237 and 0.243, respectively. The same data for Grade 4 CP-Ti is taken from [51].

The longitudinal strains measured in the 3× region of the Grade 2 CP-Ti CBT sheets at 14, 17 and 18 cycles were 0.661, 0.808 and 0.853, respectively. The maximum longitudinal strain measured in the 2×/3× necking region of the CBT sheet at 18 cycles was 1.025. As such, the longitudinal strain in the 2×/3× region in CBT is 2.25x greater than in the necked region during ST, when both sheets are very close to failure. This is significantly higher than the 1.58x increase exhibited by comparable Grade 4 CP-Ti specimens of the previous study [51] and supports the observation that higher local strains can be achieved in CBT than in ST. The longitudinal and width strains, as well as %ETF of all Grade 2 and Grade 4 CP-Ti specimens are reported in **Table 2,** along with void data discussed below.

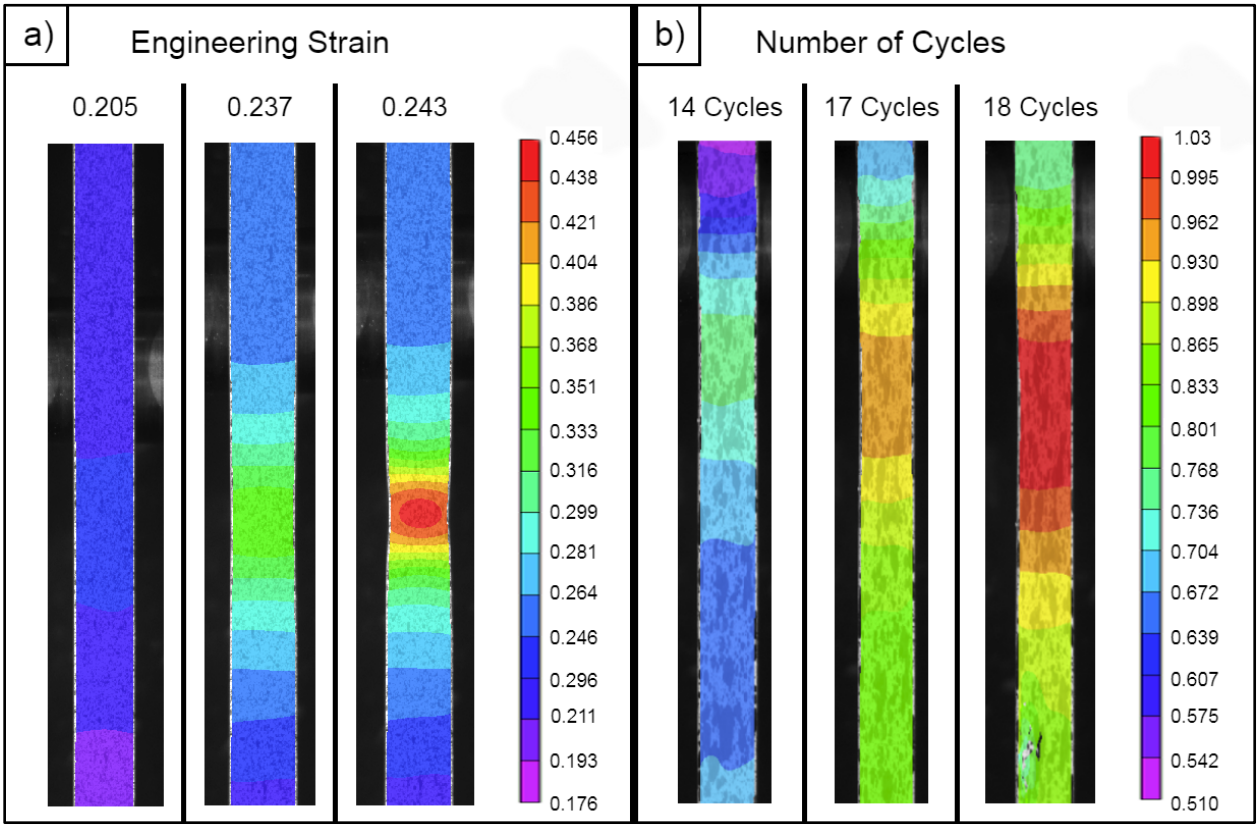

Fig. 7: Maps of Hencky major strain during (a) tensile and (b) CBT tests of Grade 2 CP-Ti sheets at the strain levels from which subsize specimens were cut.

3.2 Evolution of void density

Tomograms showing the entire through-thickness in mid-width 1mm x 1mm squares of the Grade 2 CP-Ti specimens that contained voids are shown in **Fig. 8**, with voids indicated in red. Note that the ND direction is the through-thickness direction of the sheet, and the dimension in this direction is representative of the average thickness of the entire specimen in the 3× CBT region.

Of all three Grade 2 CP-Ti ST specimens, only the G2-0.243 specimen is included in **Fig. 8**, as no voids were observed in the G2-0.205 and G2-0.237 specimens. The sudden appearance of voids is consistent with the rapid increase in longitudinal strain for the third specimen, as shown

in **Fig. 8a**. The lower strain in the necked region up to an engineering strain of 0.237 was accompanied by no observed voids; when the strain in the necked region rapidly increased to the levels shown at an engineering strain of 0.243, the region was quickly populated with voids. This contrasts with observations in the Grade 4 ST tests, where a gradual increase in void density occurred across all three ST specimens (**Table 2**) [51]. This suggests that, during monotonic tensile testing, the accumulation of voids in both grades of CP-Ti follows different patterns. The volume density of voids (ratio of total void volume to total specimen volume) in the near-failure G2-0.243 specimen was also more than twice the density of the near-failure G4-0.194 specimen. It should be noted that the expeditious failure process and related void accumulation of CP-Ti could result in significant variation in void density very near to failure (as in the G4-0.194 and G2-0.243 specimens) due to slight deviations from target strain. As such, the implication of higher critical void density of Grade 2 CP-Ti over Grade 4 CP-Ti should be considered carefully.

All of the Grade 2 CP-Ti CBT specimens contained a considerable volume of voids (**Table 2**). Interestingly, the difference in void volume density of the near-failure Grade 2 CP-Ti 18-cycle 3× and 2×/3× is much greater than the difference of the near-failure Grade 4 12-cycle 3× and 2×/3× specimens, even though the difference in longitudinal strain for both sets of specimens was similar. The Grade 2 CP-Ti 18-cycle 2×/3× specimen had 2.89x the volume density of voids of its 3× counterpart, with a difference in longitudinal strain of 14.6%. However, the Grade 4 12-cycle 2×/3× specimen had 0.98x the volume density of voids of its 3× counterpart, with a difference in longitudinal strain of 12.3%. In summary, there was a large difference in the void volume densities of the 2×/3× and 3× regions in the Grade 2 CP-Ti CBT specimens near failure, while those values were much closer in the Grade 4 CP-Ti specimens.

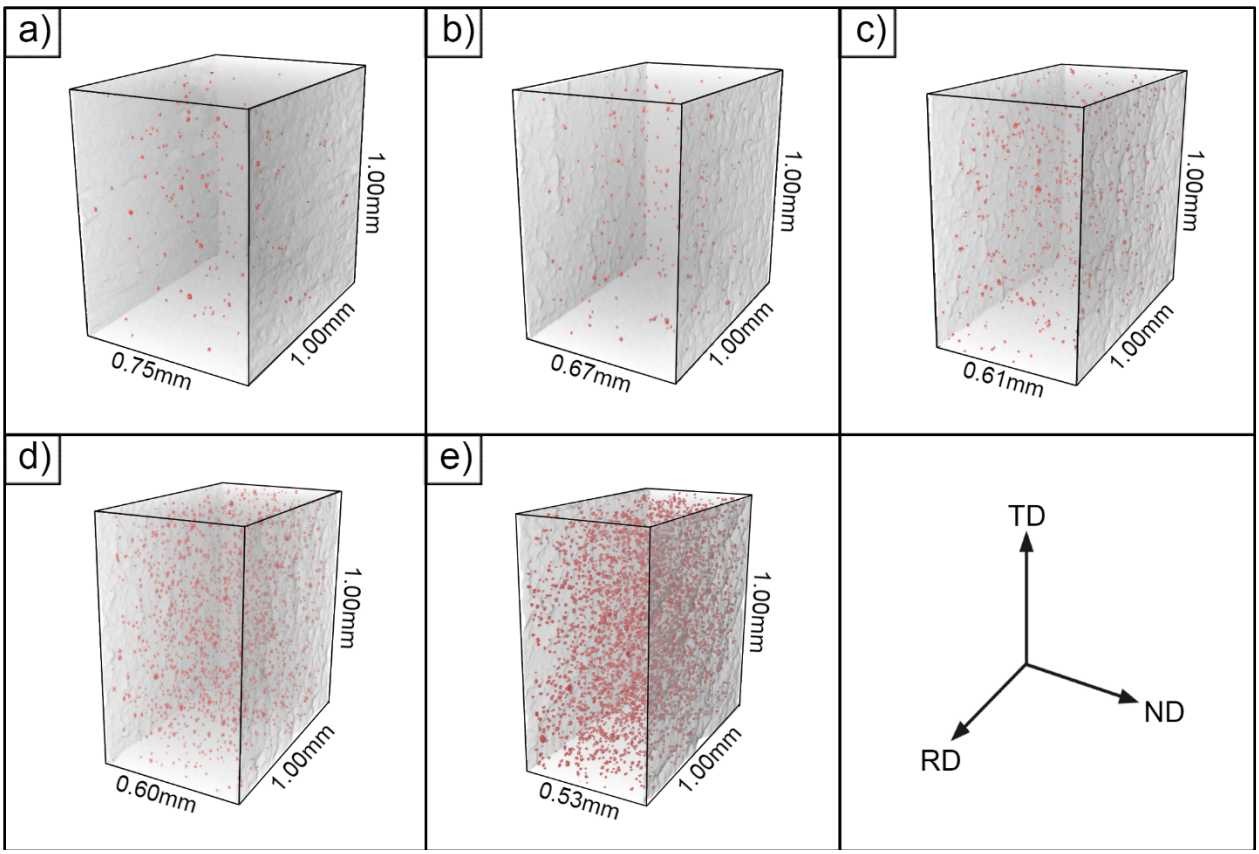

Fig. 8: Tomograms of sections from the Grade 2 CP-Ti (a) G2-0.243, (b) 14-cycle 3×, (c) 17-cycle 3×, (d) 18-cycle 3× and (e) 18-cycle 2×/3× specimen, with voids labeled in red.

To analyze the distribution of void volume density through each sheet's thickness, the tomogram of each specimen was divided into eight equal sections in the through-thickness direction (ND), and the void volume density in each section was calculated. The distributions of void volume density through the thickness of all Grade 2 and Grade 4 CP-Ti [51] specimens that contained voids, except for the G4-0.176 specimen, are shown in **Fig. 9a-d**. The G4-0.176 specimen was excluded, as this specimen contained only eighteen observable voids, resulting in questionable statistical data. The values on the horizontal axis of this plot represent the center of each section through the specimens' thickness. These plots highlight that the Grade 2 CP-Ti specimens, generally, contained a much lower void volume density than the Grade 4 CP-Ti counterparts at similar %ETFs in CBT, despite the fact that the Grade 2 CP-Ti samples experience much higher strains at these points (**Table 2**). Additionally, the shape of the distributions is somewhat different between the two alloys. The void volume density of the three 11- and 12-cycle Grade 4 CP-Ti CBT specimens clearly peaked near the center of the specimens' thickness. Near the center of the specimen, the void volume density was about 2x greater than near the edges. The distribution of void density in the Grade 2 CP-Ti CBT specimens appears to be more uniform than that of the Grade 4 CP-Ti CBT specimens, with the 18-cycle 2×/3× being the only Grade 2 CP-Ti CBT specimen to have a peak in void volume density near its center. The density in the center of this specimen was about 1.24x greater than near the edges. Both G4-0.194 and G2-0.243 specimens had a peak in density near the center of the thickness, which can be seen in the magnified version of the plots in **Fig. 9d**. The void volume density in the center of

the G4-0.194 and G2-0.243 specimens was 3x and 2.5x greater in the center than near the edges, respectively. This peak does not appear in the Grade 4 CP-Ti ST specimens at lower strains.

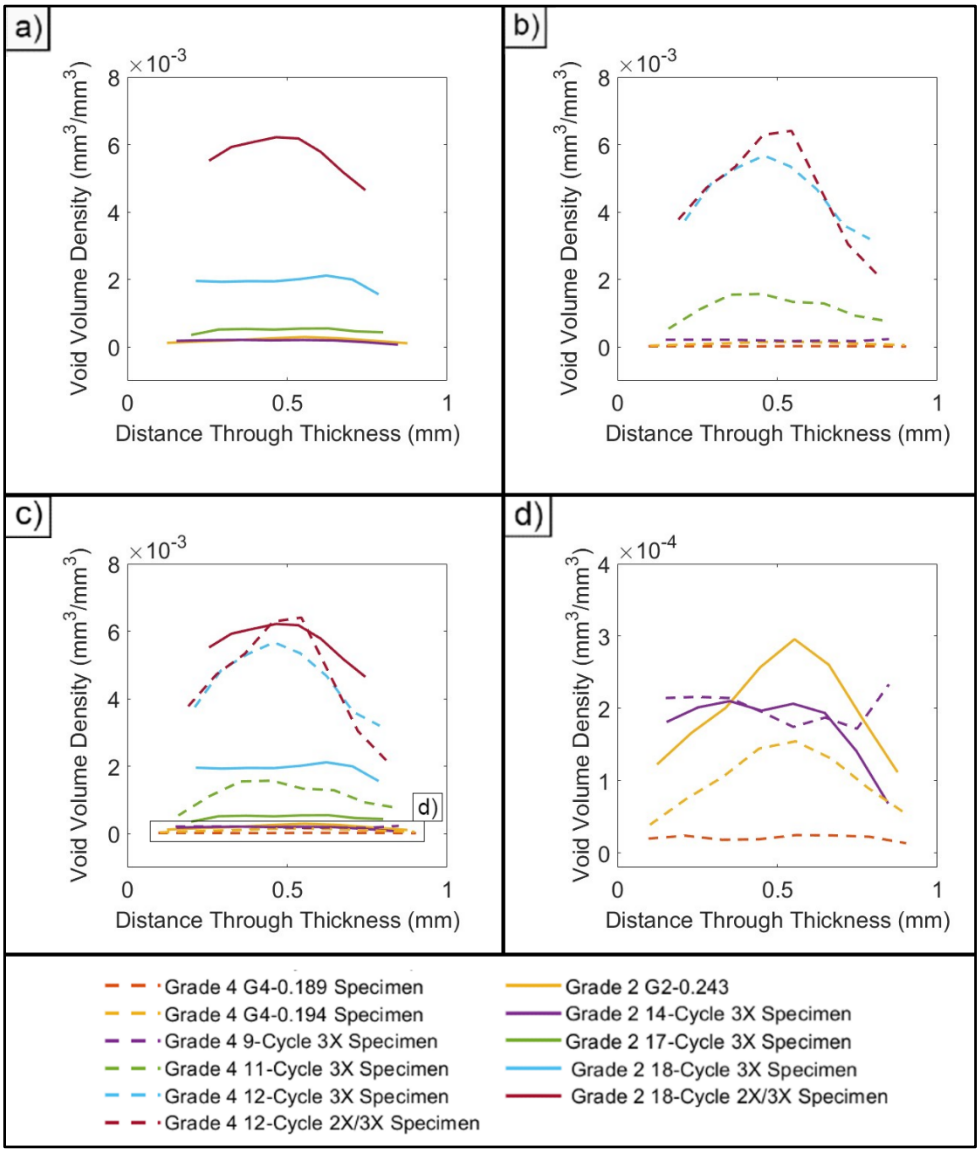

Fig. 9: Volume density of voids through the thickness of the (a) Grade 2 specimens, (b) Grade 4 specimens and (c) Grade 2 and Grade 4 specimens, as well as (d) a magnification of low-density plots indicated in (c). Note that 0.5mm on the horizontal axis represents the center of each specimen.

Table 2: ETF, void statistics, and surface strain for all Grade 2 and Grade 4 CP-Ti specimens in the study.

Specimen	Percentage ETF	Void Volume Density (mm^3/mm^3)	Void Number Density ($voids/mm^3$)	Percentage Reduction in Thickness	Average Equivalent Radius (μm)	Longitudinal Hencky Strain	Width Hencky Strain
Grade 2							
CBT - 14 Cycles, 3×	65.84%	0.0001920	250.60	31.55%	5.5	0.6611	-0.3076
CBT - 17 Cycles, 3×	86.51%	0.0005102	698.75	38.42%	5.4	0.8078	-0.3759
CBT - 18 Cycles, 3×	94.98%	0.001984	2,387.05	40.73%	5.6	0.8525	-0.3900
CBT - 18 Cycles, 2×/3×	94.98%	0.005743	6,850.63	48.56%	5.8	1.0254	-0.4412
ST – G2-0.205	82.99%	0	0	1.59%	0	0.2348	-0.1276
ST – G2-0.237	95.22%	0	0	7.67%	0	0.3471	-0.1864
ST – G2-0.245	98.52%	0.0002316	366.46	25.87%	4.8	0.4560	-0.2359
Grade 4							
CBT - 9 Cycles, 3×	68.29%	0.0002009	199.31	20.30%	6.2	0.3690	-0.1894
CBT - 11 Cycles, 3×	88.36%	0.001137	1,018.37	25.78%	6.5	0.4529	-0.2295
CBT - 12 Cycles, 3×	97.80%	0.004525	1,907.88	28.43%	7.9	0.4973	-0.2309
CBT - 12 Cycles, 2×/3×	96.95%	0.004412	2,408.64	29.01%	7.5	0.6360	-0.2887
ST – G4-0.176	83.81%	0.000004925	5.08	1.17%	6.9	0.2002	-0.1303
ST – G4-0.189	95.56%	0.00002069	26.19	9.32%	5.9	0.3298	-0.2034
ST – G4-0.194	98.04%	0.00009876	118.20	12.03%	5.8	0.3745	-0.2271

The total volume density of voids is shown with respect to the %ETF for each material and process in **Fig. 10**. Note that the data fits in **Fig. 10a** are only with respect to data of the specimens from the 3× region, although the datapoints from the 2x/3x region are also shown. The %ETF for each specimen was determined by dividing its elongation by the ETF of a sheet during a reference test. The void volume density for both materials and processes exhibited an exponential relationship with the %ETF. Relative to %ETF, the increase in void density appears to follow a very similar trend for both the Grade 2 and Grade 4 CP-Ti in CBT. However, the void volume density of most Grade 4 CP-Ti specimens was slightly higher than the Grade 2 CP-Ti specimen at a similar %ETF. The Grade 2 CP-Ti 18-cycle 2×/3× is the only exception to this.

The trends between the two materials in ST, shown in **Fig. 11b,** are more dissimilar than for CBT. Though both materials show an exponential relationship between void volume density and %ETF, the specific values reveal that significant void accumulation occurs much later in Grade 2 CP-Ti than in Grade 4 CP-Ti during ST. All three Grade 4 ST specimens showed observable voids, while the G2-0.243 specimen was the only Grade 2 CP-Ti ST specimen to contain observable voids. The void density grew steadily across the three Grade 4 ST specimens, while the onset of void accumulation was delayed in the Grade 2 ST specimens, and a sudden spike occurred close to failure.

Given the above observations in terms of the evolution of voids in CBT vs ST between Grade 2 and Grade 4 CP-Ti, the Grade 2 sheet is expected to behave much better in CBT than Grade 4 sheet but only moderately better as far as ductility in ST. Moreover, the softening behavior observed in **Fig. 5** correlates well with the evolution of voids. The softening of Grade 4 is much more pronounced than softening of Grade 2 CP-Ti.

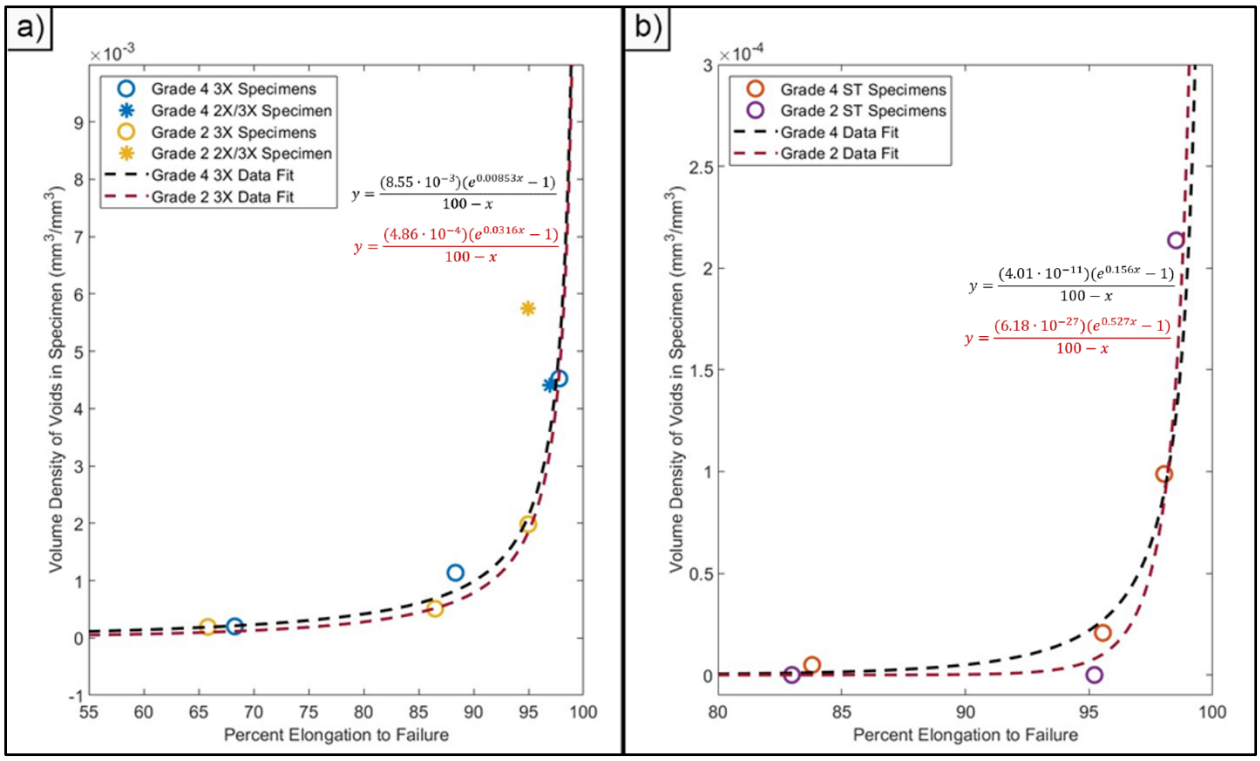

Fig. 10: Plots comparing void volume density after (a) CBT tests and (b) ST tests with exponential fits versus the %ETF.

The relationship between local longitudinal strain and void volume density for both materials is shown in **Fig. 11**. Note that the same axes were used for both subplots in **Fig. 11** to simplify visual comparison between them. With respect to longitudinal strain, the rate of increase in void volume density is higher in the Grade 4 CP-Ti than in the Grade 2 CP-Ti. This results in Grade 4 CP-Ti specimens having higher void volume density than Grade 2 CP-Ti specimens with similar values of longitudinal strain. For example, the Grade 4 CP-Ti 12-cycle 2×/3× specimen had a void volume density 22.99x higher than the Grade 2 CP-Ti 14-cycle 3× specimen, even though both specimens had a similar value of longitudinal strain. The same is true for the G2-0.243 and Grade 4 CP-Ti 11-cycle 3× specimens, where the latter had a 4.91x

higher void volume density than the former. This trend of faster void accumulation in Grade 4 CP-Ti is further highlighted by the two data fits in **Fig. 11**. The slope of the linear exponent in the data fit for Grade 4 CP-Ti is 9.99, while that of the Grade 2 CP-Ti is 3.43. This exemplifies the greater rate of void accumulation in Grade 4 CP-Ti.

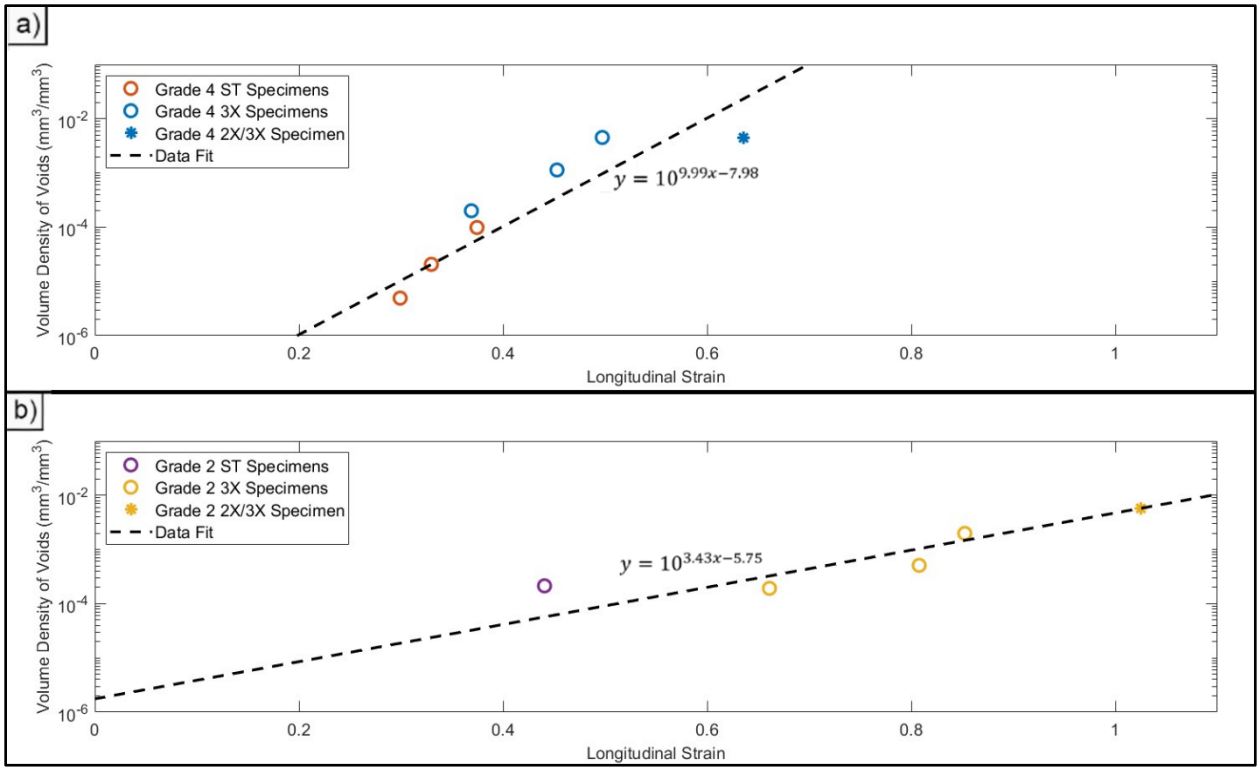

Fig. 11: Semi-logarithmic plots of void volume density versus longitudinal strain in (a) Grade 4 CP-Ti specimens and (b) Grade 2 CP-Ti specimens with base-ten exponential fits of the data.

At similar %ETFs, the volume density of voids was significantly higher in the Grade 4 CP-Ti specimens than in the Grade 2 CP-Ti specimens, except for the G2-0.243 and 18-cycle 2×/3×. However, the *number* density of voids (ratio of number of observed voids to specimen volume) in the Grade 2 CP-Ti specimens was generally higher when compared at similar %ETFs (**Table 2**). In particular, the Grade 2 18-cycle 3× specimen had a number density of voids 1.25x higher than the Grade 4 12-cycle 3× specimen, where both were at similar %ETFs. This is also shown in the 2×/3× specimens of each alloy, with the Grade 2 CP-Ti specimen having a 2.84x greater number density of voids than its Grade 4 CP-Ti counterpart.

Analyzing void number density with respect to %ETF does not consider the higher local strains achieved by Grade 2 CP-Ti. Void number densities with respect to longitudinal strain are shown in **Fig. 12**. Note that the same axes are used in both subplots to facilitate comparisons. When compared at similar strains, rather than similar %ETFs, the void number densities are significantly lower in Grade 2 CP-Ti. This is exemplified by comparing the Grade 2 14-cycle 3× and Grade 4 12-Cycle 2×/3× specimens. At similar levels of longitudinal strain, the Grade 4 12-Cycle 2×/3× specimen had a 9.61x greater number density of voids than the Grade 2 14-cycle 3× specimen. Additionally, the Grade 2 18-cycle 3× specimen and the Grade 4 12-cycle 2×/3× specimen had a similar number density of voids, even though the longitudinal strain in the Grade 2 18-cycle 3× specimen was 1.71x greater. This shows that the rate of void accumulation, in

terms of volume density, is at least partially due to a lower rate of increase in the number of observable voids. This fact is also born out in the exponential data fits of **Fig. 12**. The slope of the exponent in the Grade 4 CP-Ti data fit is 13.48, while that of the Grade 2 CP-Ti is 8.75, demonstrating the more rapid increase in void number density with respect to longitudinal strain.

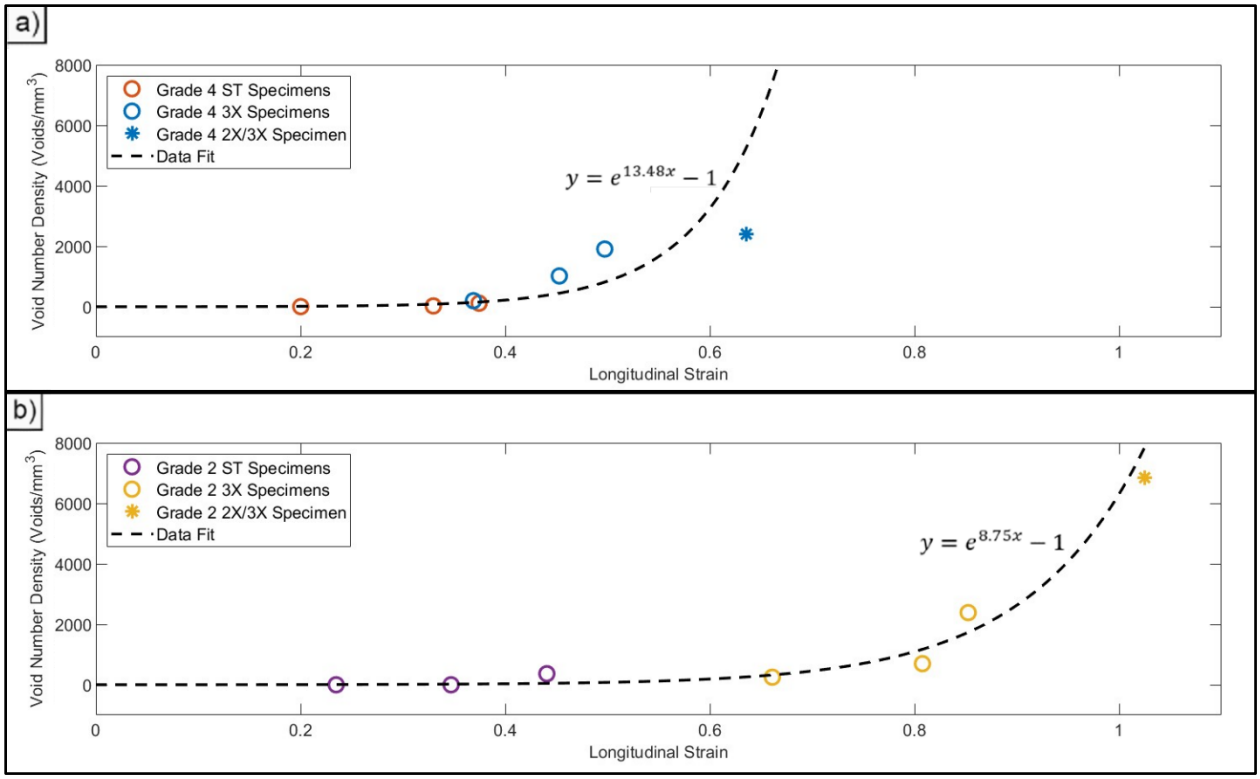

Fig. 12: Plots of void number density versus longitudinal strain in (a) Grade 4 CP-Ti specimens and (b) Grade 2 CP-Ti specimens with exponential fits of the data.

3.3 Evolution of void size

Analysis of void size revealed further differences in void evolution of the two CP-Ti alloys. Void size was quantified using an equivalent radius, which is the radius of a sphere that has the same volume as the void being observed. The distribution of void sizes through each specimen's thickness was determined in a manner similar to the void volume density through the thickness shown in **Fig. 9**. The tomogram of each specimen was divided into eight sections of equal size, and the equivalent radii of the voids in each section were averaged, resulting in the average equivalent radius. The average equivalent radii through the thickness of the CBT specimens are shown in **Fig. 13a** and the ST specimens in **Fig. 13b**, where the horizontal axis represents the center of each section. Again, the G4-0.176 specimen was excluded due to the small number of voids observed, and the G2-0.205 and G2-0.237 specimens are not shown, as neither contained any observable voids. For both materials, the void size is relatively uniform through the thickness of all of the specimens.

To compare the void size between specimens, the overall average equivalent radius, shown in **Table 2**, was determined by averaging the equivalent radii of all voids in each specimen. The relationship between overall average void size and longitudinal strain for all of the specimens is plotted in **Fig. 14**. Note that the same axes were used for both subplots in **Fig. 14** to simplify

visual comparison between the two datasets. From this, it is clear that there is much more void growth in Grade 4 CP-Ti throughout the CBT process than in the Grade 2 CP-Ti. In Grade 4 CP-Ti, the average void size increased by 1.7μm in the 3× region from 9 to 12 cycles. A much smaller increase in void size occurred in the Grade 2 CP-Ti CBT sheets, with the void size increasing by only 0.1μm in the 3× from 14 to 18 CBT cycles. Furthermore, the maximum average void size of the Grade 2 CP-Ti CBT specimens was found in the 18-cycle 2×/3× specimen at 5.8μm. The minimum overall average void size of the Grade 4 CP-Ti CBT specimens was 6.2μm, 0.4μm larger than the largest average size of the Grade 2 CBT specimens. A similar difference is shown in the ST specimens. The G4-0.189 and G4-0.194 specimens had an average void size of 5.9μm and 5.8μm, respectively, while the G2-0.243 specimen had an average void size of 4.8μm. This shows that void growth is prominent in Grade 4 CP-Ti, while it is less-so in the Grade 2 CP-Ti. This can be further understood by observing the linear fits for both data sets in **Fig. 14**. The slope of the linear fit for the Grade 4 CP-Ti data is 6.43, representing the significant increase in overall average void size with increasing longitudinal strain. The minimal void growth observed in the Grade 2 CP-Ti is reflected by its linear fit having a slope of only 0.88.

Fractography was performed on Grade 2 CP-Ti samples failed in both CBT and ST. Images of the fracture surfaces are shown in **Fig 15**. No increase in average dimple size towards the center of the fracture surface of Grade 2 CP-Ti was evident in either specimen. This contrasts the findings from fractography of Grade 4 CP-Ti in the previous study [51]. This is consistent with the near-uniform distribution of void density through the thickness of the Grade 2 CP-Ti CBT samples shown in **Fig. 9.**

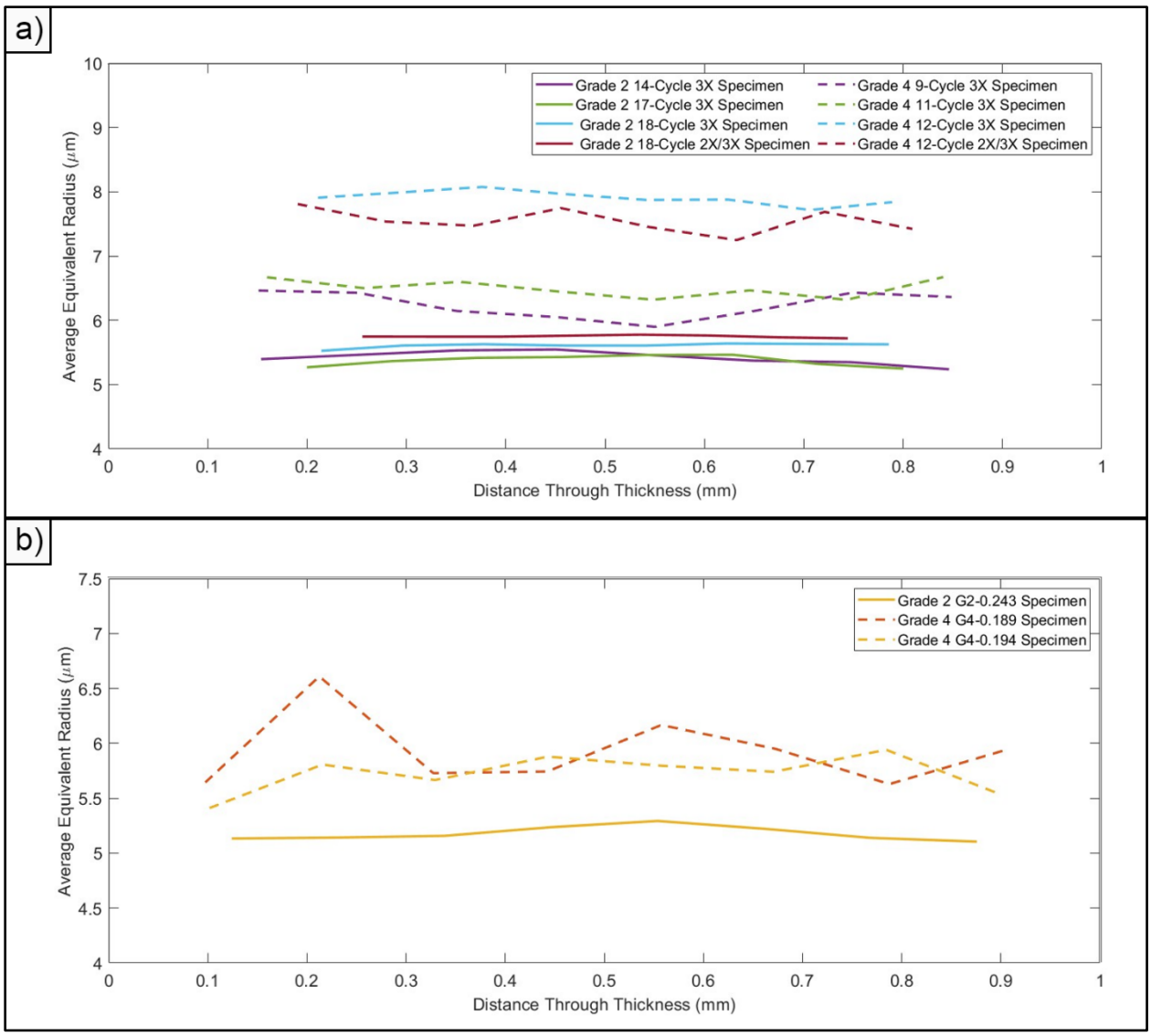

Fig. 13: Average equivalent radius of through the thickness of the (a) Grade 2 and Grade 4 CBT specimens and (b) Grade 2 and Grade 4 ST specimens. Note that 0.5mm on the horizontal axis represents the center of each specimen.

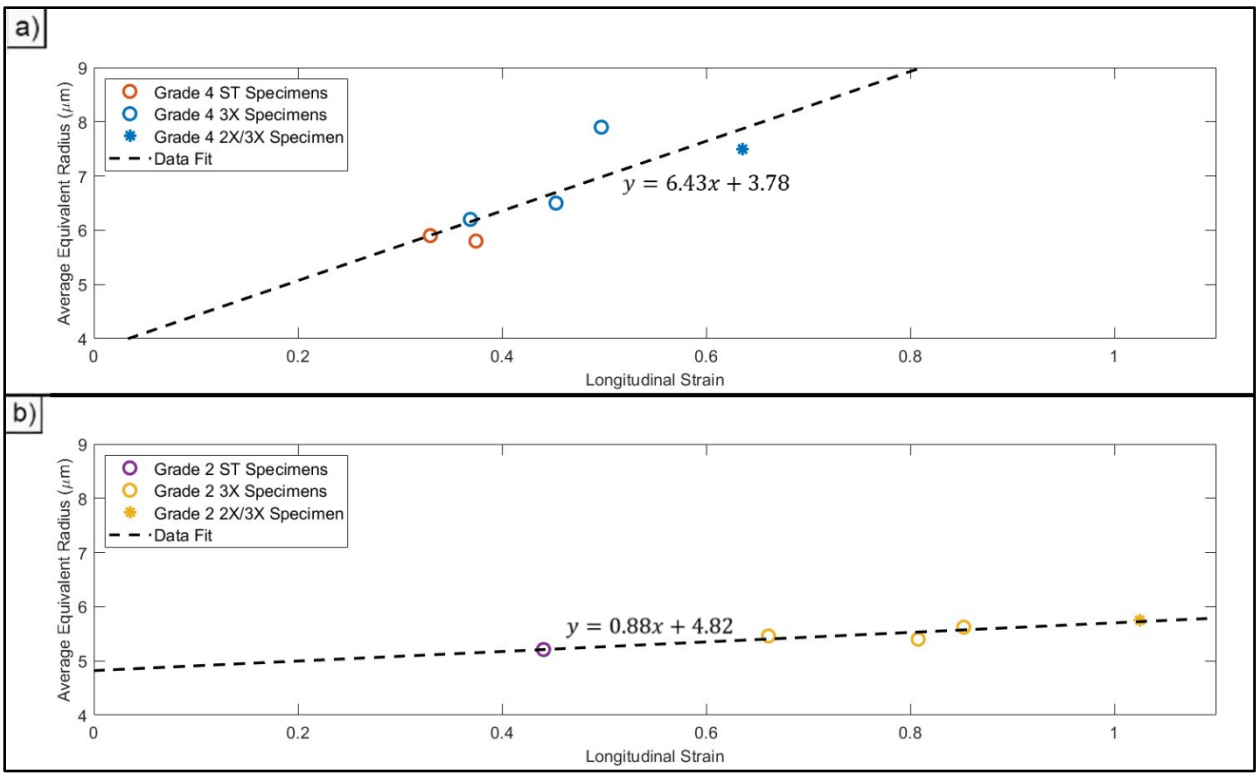

Fig. 14: Plot showing average equivalent radius of voids in the entirety of the (a) Grade 4 CP-Ti specimens and (b) Grade 2 CP-Ti specimens with linear fits of the data.

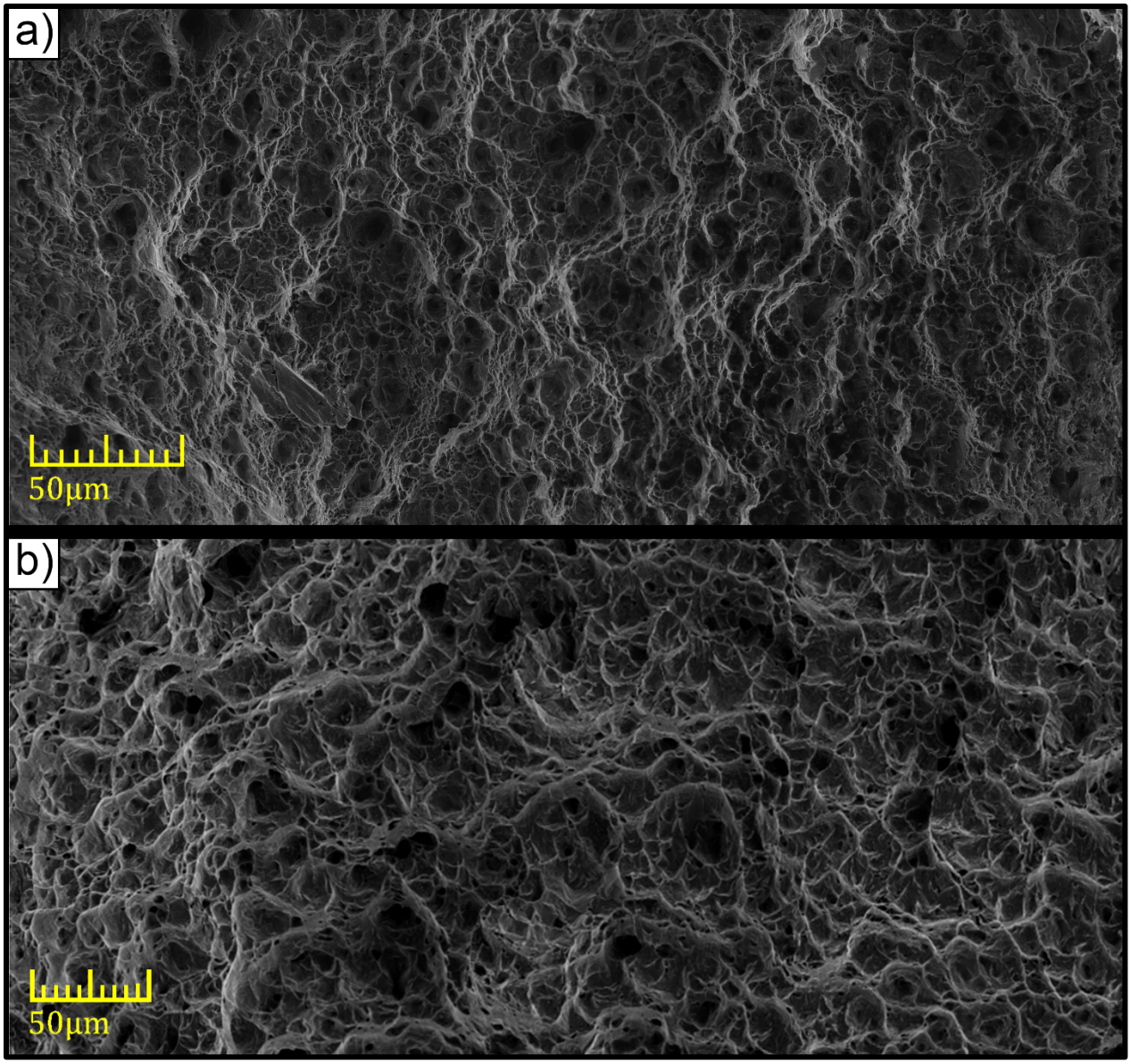

Fig. 15: Images showing the fracture surface of post-mortem Grade 2 CP-Ti after (a) CBT and (b) ST

3.4 Grain structure revealed via electron backscatter diffraction

In closing this section, inverse pole figure (IPF) maps obtained using EBSD in RD-ND planes of Grade 2 and Grade 4 CP-Ti sheets are shown in **Fig. 16**. The scans of the initial (undeformed) Grade 2 and Grade 4 CP-Ti are shown in **Fig. 16a-b**. The initial microstructures largely consisted of equiaxed grains that are slightly bigger in Grade 4 than Grade 2. The area-averaged grain diameter and aspect ratio of the initial Grade 2 CP-Ti were 9.79μm and 0.50, respectively, and those of the initial Grade 4 CP-Ti were 10.96μm and 0.51. The IPF maps in **Fig. 16c-d** show the microstructure in the 3× region of Grade 2 and Grade 4 CP-Ti after 14 CBT cycles and 11 CBT cycles. The alloys were observed at these two levels of deformation due to their similar %ETFs. More grain fragmentation occurred in the Grade 2 CP-Ti CBT specimen, likely due to the greater strains imposed. The area-averaged grain diameter of the Grade 2 CP-Ti

CBT specimen decreased to 6.56μm after 14 CBT cycles, while the average grain diameter of the Grade 4 CP-Ti CBT specimen did not change appreciably, signifying very little change in grain size. The average grain aspect ratio was similar for both alloys, at 0.39 and 0.38 in the Grade 2 and Grade 4 CP-Ti CBT specimens.

$\{10\bar{1}2\}$, $\{11\bar{2}1\}$, $\{11\bar{2}2\}$, $\{10\bar{1}1\}$ twin boundaries in the Grade 2 and Grade 4 CP-Ti CBT specimens are highlighted in the grain maps of **Fig. 16c'-d'**. These maps show that Grade 2 CP-Ti has a greater propensity for deformation twinning than Grade 4 CP-Ti. The greater extent of twinning exhibited by Grade 2 CP-Ti likely aids in its ability to achieve greater elongations than Grade 4 CP-Ti, in CBT.

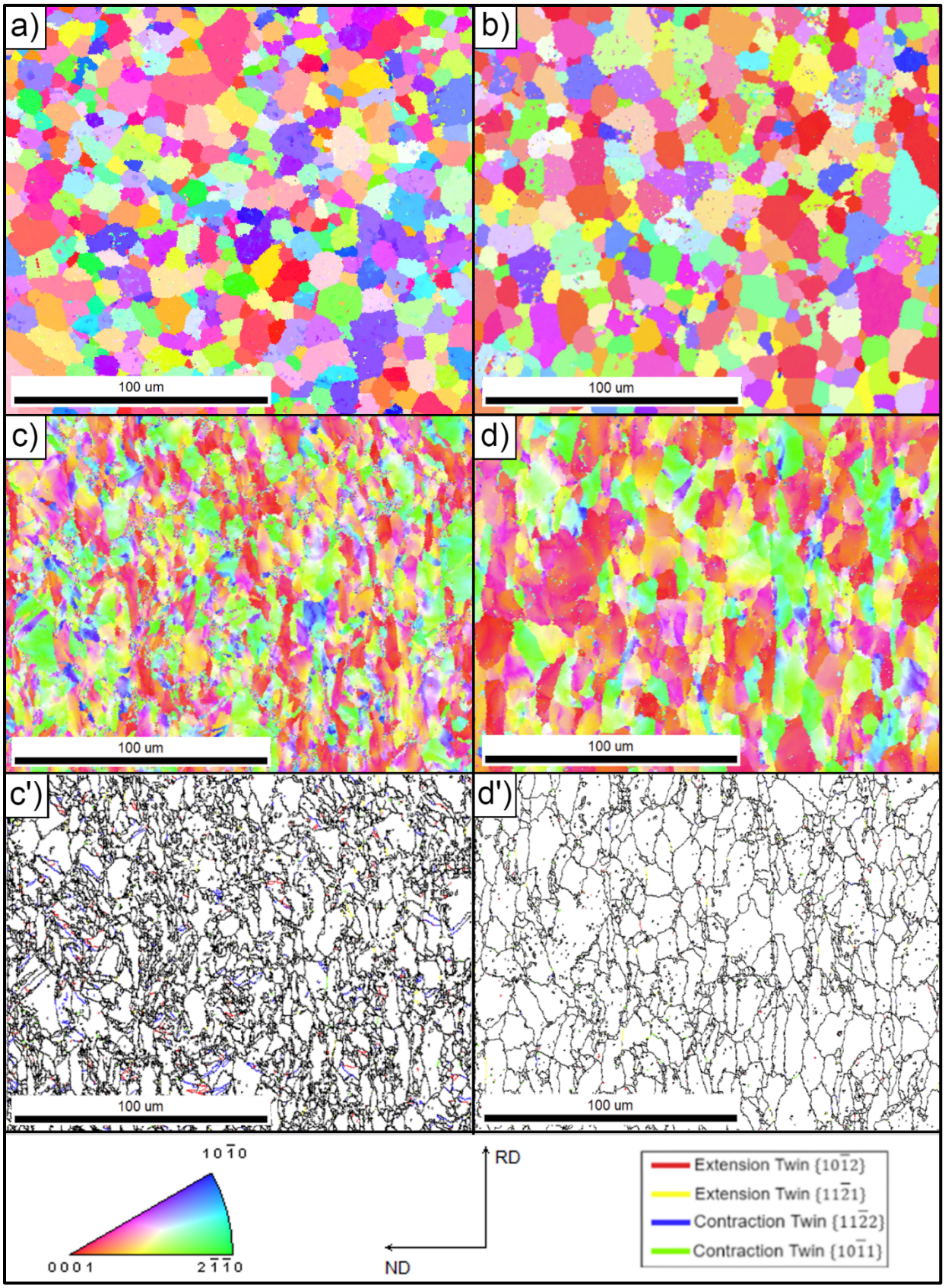
a)
100 um
b)
100 um
c)
100 um
d)
100 um
c')
100 um
d')
100 um
$10\bar{1}0$
0001
$2\bar{1}\bar{1}0$
RD
ND
Extension Twin $\{10\bar{1}2\}$
Extension Twin $\{11\bar{2}1\}$
Contraction Twin $\{11\bar{2}2\}$
Contraction Twin $\{10\bar{1}1\}$

Fig. 16: Inverse pole figure (IPF) maps of (a) initial Grade 2 CP-Ti, (b) initial Grade 4 CP-Ti, (c) Grade 2 CP-Ti after 14 CBT cycles in 3× region, (d) Grade 4 CP-Ti after 11 CBT cycles in 3× region and grain maps highlighting twin boundaries of (c) and (d) in (c') and (d'). The colors in the IPF maps represent crystal orientations relative to the TD sample axis according to the colors in the standard triangle.

4. Discussion

This investigation has shown the mechanical response of Grade 2 CP-Ti in both CBT and ST. The mechanical response was compared to results of Grade 4 CP-Ti from our previous investigation [51]. The size, density and fraction of voids in the Grade 2 CP-Ti were investigated using XCT, and these results were also compared to the previous investigation involving Grade 4 CP-Ti. The grain structures of the initial materials and after CBT to a certain number of CBT cycles were also revealed by EBSD.

The difference in mechanical response of the Grade 2 CP-Ti sheet, compared to the Grade 4 CP-Ti sheet, is remarkable. The elongation in Grade 4 CP-Ti sheets in CBT was shown to be 2.37x greater than in ST in our previous investigation [51]. In contrast, the ETF of Grade 2 CP-Ti in CBT was 4.4x greater than in ST. This is even more notable when considering that the ductility of Grade 2 CP-Ti in ST is only 1.24x greater than Grade 4 CP-Ti in ST. The higher strength and lower ductility of Grade 4 CP-Ti can be attributed to its increased oxygen content, which is 0.25% compared to 0.09% in Grade 2 CP-Ti (**Table 1**). Increases in oxygen content have been shown to increase the strength and decrease the ductility of Ti alloys [54-58]. Chong et al. [56] showed that the ductility of high-purity Ti was 3x higher than Ti with 0.3wt% oxygen (Ti-0.3wt%O), with high-purity Ti failing at an engineering strain of 0.48 and Ti-0.3wt%O failing at an engineering strain of 0.16. The yield strength of Ti-0.3wt% was found to be 472MPa, 3x higher than the yield strength of the high-purity Ti. In the current study, this effect is likely exacerbated by incremental nature of CBT.

It was shown that observable voids were present at significantly lower levels of strain in Grade 4 CP-Ti than in Grade 2 CP-Ti (**Fig. 10**). Voids were observed at an engineering strain of 0.176 in the neck of a Grade 4 CP-Ti sheet after tensile testing, while voids were not observed in the Grade 2 CP-Ti sheet until an engineering strain of 0.243. The observation of voids at lower strains in Grade 4 CP-Ti could be due to multiple factors. First, lower ductility and higher strength of Grade 4 CP-Ti (**Fig. 5)** suggests less dislocation mobility during large plastic deformation [88-90]. Immobile dislocations can result in dislocation pile-ups, which often occur at grain boundaries, twin boundaries and impurities [91-93]. These can reorganize into dislocation blocks and cells [94, 95]. The high hydrostatic stresses at these boundaries promote vacancy condensation, resulting in the formation of voids [71, 96, 97]. Thus, the lower mobility of dislocations in Grade 4 CP-Ti would likely result in a large number of dislocation pile-ups at lower strains than in Grade 2 CP-Ti. The inhibition to dislocation mobility posed by oxygen interstitials in Ti have been observed through in-situ TEM imaging of Ti nanopillars with varying oxygen content deformed in compression by Yu et al [98]. It was shown that oxygen interstitials present a barrier to dislocation glide, and cause pinning of screw dislocations. These insights provide an explanation for a direct relationship between increased oxygen content and the more rapid damage accumulation observed in Grade 4 CP-Ti. Additionally, the nature of impurities resulting from the higher oxygen content of the Grade 4 CP-Ti could contribute to the earlier development of observable voids. Studies have shown that the size and number of

inclusions in a metallic matrix increase with an increase in oxygen content [99-101]. For example, Seo et al [101] observed that the size of oxide inclusions increased by about 1.5x and their number density increased by about 4x when the oxygen content in bainitic welds increased from 100 to 300ppm**.** Furthermore, it has been shown that increasing inclusion size lowers the void nucleation strain in various materials [76, 81, 102]. A study by Cox and Low [81] investigated the dependence of void nucleation strain on inclusion size and stress triaxiality in both notched and smooth 18-Ni 200 Grade maraging steel and AISI 4340 steel. It was found that the void nucleation strain decreased with an increase in inclusion size, while the nucleation strain was independent of stress triaxiality. However, it was found that the rate of void *growth* increased with stress triaxiality, with voids growing at a greater rate in the notched specimen than in the round specimen.

When compared at similar %ETFs, the number density of voids in the Grade 2 CP-Ti specimens is consistently higher than in the Grade 4 CP-Ti specimens (**Table 2**). This comparison, however, does not account for larger strains achieved by the Grade 2 CP-Ti sheets, especially in CBT. At similar levels of strain, the number of voids in the Grade 4 CP-Ti specimens was much larger than in the Grade 2 CP-Ti specimens (**Fig. 12**). This is consistent with data shown by Horstemeyer and Gokhale [78], who showed that the number density of voids at a given strain, in different materials, decreased with an increase in ductility. Increased porosity has been repeatedly demonstrated to decrease the ductility and fatigue strength of materials [103-109]. As such, the lower void density in Grade 2 CP-Ti at similar strains to the Grade 4 CP-Ti results in greater integrity of the material, allowing for further plastic deformation to occur. Additionally, the specimens extracted from the 2×/3× interface of the near-failure sheets after CBT were subject to the greatest strains and contained the highest volume density of voids for their respective alloy. This is the result of the large amount of plastic deformation occurring above the inner-most roller at the end of each pass during CBT. This eventually results in localization and subsequent failure in this region.

The smaller size of voids in the Grade 2 CP-Ti, compared to the Grade 4 CP-Ti, is notable. The size of voids in the Grade 2 CP-Ti were consistently smaller than those of the Grade 4 CP-Ti, independent of %ETF or strain. In the ST specimens, the Grade 4 CP-Ti exhibited a decrease in average void size with increased strain, due to the relatively small number of voids in the G4-0.176 and G4-0.189 specimens (**Table 2**). Since voids were only observed in one Grade 2 CP-Ti specimen after ST, a comparison of void size in the two alloys in ST cannot be made. An apt comparison can be made for the two alloys in CBT, however. In the Grade 4 CP-Ti CBT specimens, the size of the voids increased with each subsequent cycle, and thus, increasing strain (**Figs. 13-14**). The only exception to this is between the Grade 4 12-cycle 3× and 2×/3× specimens, where the voids were slightly smaller in the 2×/3× region, despite higher longitudinal strain. The Grade 2 CP-Ti only exhibited a minimal increase in average void size during CBT. This lack of void growth results in Grade 2 CP-Ti CBT specimens with a higher number density of voids having a lower volume density compared to the Grade 4 CP-Ti CBT specimens. To explain the mechanisms behind the inhibited void growth in Grade 2 CP-Ti, detailed microstructural analysis that is out of the scope of this study is required. However, this may be motivation for a future work on this topic. Less void growth in Grade 2 CP-Ti undoubtedly aids in achieving such high strains in CBT due to the lower density and decreased stress concentration surrounding individual voids. For example, stress concentrations surrounding voids were investigated through models performed by Davis et al. [110]. The study found that stress immediately surrounding the voids did not depend on the size of the voids, but larger voids

distributed stress to greater distances than smaller voids. This suggests that, on average, the ligaments between voids in the Grade 2 CP-Ti specimen would be less likely to rupture than in the Grade 4 CP-Ti specimens due to the voids' smaller average size. The behavior of voids governed the flow softening behavior shown in **Fig. 5**.

The extent of microstructural deformation exhibited by the Grade 2 and Grade 4 CP-Ti after CBT is shown in the EBSD scans of **Fig. 16**. In the 3× region, after 14 CBT cycles, the high level of plastic deformation is accompanied by significant amounts of grain fragmentation and twinning that are not shown in Grade 4 CP-Ti at a similar %ETF in CBT. The greater propensity of Grade 2 CP-Ti to produce deformation twins is consistent with the findings of other works [56, 111, 112]. This has been attributed to oxygen interstitials segregating to $\{10\bar{1}2\}$, $\{11\bar{2}1\}$ and $\{10\bar{1}1\}$ twin boundaries, consequently pinning them and inhibiting the twins' growth [56]. The activation of twin systems in Grade 2 CP-Ti provides another deformation mode for the alloy to accommodate large plastic strains [113-115]. In addition to slower damage accumulation, the propensity of Grade 2 CP-Ti to produce deformation twins likely aids in its ability to achieve greater elongations in CBT, compared to Grade 4 CP-Ti. In the Grade 2 CP-Ti, the large amount of grain fragmentation may contribute to the void volume density in the 2×/3× interface that is substantially larger than that in the 3× region. The higher strain in the 2×/3× interface results in a large number of voids suddenly growing close to failure. It is possible that the lack of grain fragmentation at large strains in Grade 4 CP-Ti does not provide the many preferable void nucleation sites that are afforded in Grade 2 CP-Ti, resulting in a closer void volume density between the 2×/3× interface and 3× region in Grade 4 CP-Ti near failure. However, further extensive investigation is necessary to determine the mechanism behind this.

5. Conclusions

This paper serves as a follow-up to our previous publication on the investigation of damage accumulation in Grade 4 CP-Ti in ST and CBT by comparing the results to Grade 2 CP-Ti. From the current investigation, the following conclusions can be drawn:

- CBT processing is much more beneficial to the increased elongation of Grade 2 CP-Ti than Grade 4 CP-Ti. The ETF of Grade 4 CP-Ti in CBT was 2.5x greater than in ST, while the ETF of Grade 2 CP-Ti in CBT was 4.4x greater than in ST. This is remarkable considering that, in ST, the ETF of Grade 2 CP-Ti is only 1.2x greater than Grade 4 CP-Ti. Hence, only part of the increased elongation during CBT is owed to the increased ductility of Grade 2 CP-Ti compared with Grade 4 CP-Ti. Before failure during CBT, the local longitudinal strains in Grade 2 CP-Ti were 1.9x greater in the 3× region and 1.7x greater in the 2×/3× region than in Grade 4 CP-Ti. The unknown additional mechanisms behind the substantial increase in elongation of Grade 2 CP-Ti over Grade 4 CP-Ti were a significant motivation behind this study. Based upon the results presented here, it is likely that the much slower damage accumulation exhibited by Grade 2 CP-Ti plays a large role in delaying failure. Additionally, the formation of deformation twins likely aids in increasing the ductility of Grade 2 CP-Ti.
- Voids that are observable by XCT develop much earlier in Grade 4 CP-Ti than in Grade 2 CP-Ti during ST. Additionally, the Grade 2 CP-Ti fails soon after observable voids

develop, while the nucleation and growth of voids is more gradual during tensile deformation of Grade 4 CP-Ti. Voids were first observed in the Grade 4 CP-Ti during ST at an engineering strain of 0.176, while the engineering strain at failure was 0.198. In contrast, voids were first observed in Grade 2 CP-Ti at an engineering strain of 0.243, and the engineering strain at failure was 0.246.

- The void content prior to failure is much higher in CBT than in ST for both alloys. In CBT, Grade 4 CP-Ti was able to achieve a void volume density 45.8x greater than in ST. The Grade 2 CP-Ti in CBT reached a void volume density 24.8x greater than in ST despite Grade 2 achieving much greater ETF in CBT than Grade 4. This reinforces the previous finding that CBT does not delay void nucleation and growth but increases the ETF of materials despite large amounts of damage accumulation. CBT postpones coalescence of voids, allowing a greater volume of voids before failure. The flow softening behavior CBT vs ST of Grade 4 vs Grade 2 CP-Ti correlated with the evolution of voids.
- In CBT, the Grade 4 CP-Ti accumulates a greater number density of voids than the Grade 2 CP-Ti at similar strain levels. The slower rate of void nucleation with respect to longitudinal strain aids in the greater ETF of Grade 2 CP-Ti. However, the number density of voids achieved prior to failure is 2.8x greater in Grade 2 CP-Ti than in Grade 4 CP-Ti.
- The voids in Grade 4 CP-Ti are significantly larger on average than those in the Grade 2 CP-Ti, with the maximum average equivalent radius being 7.9μm in Grade 4 CP-Ti and 5.8μm in Grade 2 CP-Ti. Furthermore, a significant increase in the average equivalent radius of voids occurs in Grade 4 CP-Ti with each subsequent CBT cycle, while very little change in average void size occurs in the Grade 2 CP-Ti during CBT. In addition to the slower rate of void nucleation, the inhibited void growth in Grade 2 CP-Ti also contributes to its increased ETF over Grade 4 CP-Ti.
- The distribution of void volume density differs between the two alloys. Close to failure in ST, a peak in void volume density occurs near the center of the sheet thickness in both alloys. In the Grade 4 CP-Ti, the void volume density is about 2.5x greater in the center than at the edges, and in Grade 2 CP-Ti, the void volume density is about 3x greater in the center than at the edges. During CBT, this peak forms at 11 CBT cycles in Grade 4 CP-Ti, with the void density in the center being about 2x greater than at the edges and is present in both the 3× and 2×/3× regions. A slight peak develops in the 2×/3× region of the Grade 2 CP-Ti sheet after 18 CBT cycles, with the void density being only 1.2x greater in the center than at the edges.
- Greater twinning and grain fragmentation is present in the Grade 2 CP-Ti than Grade 4 CP-Ti after CBT. The ability of Grade 2 CP-Ti to more readily create deformation twins than Grade 4 CP-Ti likely plays a role in the greater elongation that it achieves during CBT.

Acknowledgements
The BYU and UNH teams were supported by NSF grants CMMI 2147126 and CMMI 2147122 respectively. SEM microscopy research reported in this publication was supported with funds awarded to UNH from the US National Science Foundation (NSF) (MRI grant 1337897; Todd Gross, Mechanical Engineering, UNH, PI) and funds from UNH. Philip Noell was supported by

a Laboratory Directed Research and Development (LDRD) program. Sandia National Laboratories is a multi-mission laboratory managed and operated by National Technology and Engineering Solutions of Sandia LLC, a wholly owned subsidiary of Honeywell International Inc., for the U.S. Department of Energy's National Nuclear Security Administration under contract DE-NA0003525. The views expressed in the article do not necessarily represent the views of the U.S. Department of Energy or the United States Government.

Data availability

The raw/processed data required to reproduce these findings cannot be shared at this time due to technical or time limitations.

References

[1] M. Patel, B. Pardhi, S. Chopara, M. Pal, Lightweight composite materials for automotive-a review, Carbon 1(2500) (2018) 151.
[2] F. Czerwinski, Current Trends in Automotive Lightweighting Strategies and Materials, Materials (Basel) 14(21) (2021).
[3] W. Zhang, J. Xu, Advanced lightweight materials for Automobiles: A review, Materials & Design 221 (2022) 110994.
[4] A. Bravo, D. Vieira, G. Ferrer, Emissions of future conventional aircrafts adopting evolutionary technologies, J Clean Prod 347 (2022) 131246.
[5] L. Zhu, N. Li, P.R.N. Childs, Light-weighting in aerospace component and system design, Propulsion and Power Research 7(2) (2018) 103-119.
[6] J. Lee, J. Mo, Analysis of technological innovation and environmental performance improvement in aviation sector, Int J Environ Res Public Health 8(9) (2011) 3777-95.
[7] J.J. Lee, S.P. Lukachko, I.A. Waitz, A. Schafer, Historical and future trends in aircraft performance, cost, and emissions, Annual Review of Energy and the Environment 26(1) (2001) 167-200.
[8] J. Hüffmeier, M. Johanson, State-of-the-Art Methods to Improve Energy Efficiency of Ships, Journal of Marine Science and Engineering 9(4) (2021) 447.
[9] L. Mishnaevsky, K. Branner, H.N. Petersen, J. Beauson, M. McGugan, B.F. Sørensen, Materials for Wind Turbine Blades: An Overview, Materials (Basel) 10(11) (2017).
[10] T.M. Rust, W.G. Steltz, Titanium for Steam Turbine Blades, JOM 34(9) (1982) 42-47.
[11] E. Quaranta, P. Davies, Emerging and Innovative Materials for Hydropower Engineering Applications: Turbines, Bearings, Sealing, Dams and Waterways, and Ocean Power, Engineering 8 (2022) 148-158.
[12] F. Lionetto, Carbon Fiber Reinforced Polymers, Materials, 2021.
[13] Y.F. Khalil, Eco-efficient lightweight carbon-fiber reinforced polymer for environmentally greener commercial aviation industry, Sustainable Production and Consumption 12 (2017) 16-26.
[14] P. Morampudi, K.K. Namala, Y.K. Gajjela, M. Barath, G. Prudhvi, Review on glass fiber reinforced polymer composites, Materials Today: Proceedings 43 (2021) 314-319.
[15] D.K. Rajak, P.H. Wagh, E. Linul, Manufacturing Technologies of Carbon/Glass Fiber-Reinforced Polymer Composites and Their Properties: A Review, Polymers 13(21) (2021) 3721.

[16] T. Sathishkumar, S. Satheeshkumar, J. Naveen, Glass fiber-reinforced polymer composites – a review, Journal of Reinforced Plastics and Composites 33(13) (2014) 1258-1275.
[17] J. Min, J. Hu, C. Sun, H. Wan, P. Liao, H. Teng, J. Lin, Fabrication processes of metal-fiber reinforced polymer hybrid components: a review, Advanced Composites and Hybrid Materials 5(2) (2022) 651-678.
[18] S. Sajan, D. Philip Selvaraj, A review on polymer matrix composite materials and their applications, Materials Today: Proceedings 47 (2021) 5493-5498.
[19] M. Hockauf, M.F.-X. Wagner, M. Händel, T. Lampke, S. Siebeck, B. Wielage, High-strength aluminum-based light-weight materials for safety components – recent progress by microstructural refinement and particle reinforcement, International Journal of Materials Research 103(1) (2012) 3-11.
[20] S. Amirkhanlou, S. Ji, Casting lightweight stiff aluminum alloys: a review, Critical Reviews in Solid State and Materials Sciences 45(3) (2020) 171-186.
[21] T. Abbott, M. Easton, R. Schmidt, Magnesium for Crashworthy Components, in: S.N. Mathaudhu, A.A. Luo, N.R. Neelameggham, E.A. Nyberg, W.H. Sillekens (Eds.), Essential Readings in Magnesium Technology, Springer International Publishing, Cham, 2016, pp. 463-466.
[22] A. Tharumarajah, P. Koltun, Is there an environmental advantage of using magnesium components for light-weighting cars?, Journal of Cleaner Production 15(11) (2007) 1007-1013.
[23] A.A. Luo, Recent advances in light metals and manufacturing for automotive applications, CIM Journal 12(3) (2021) 79-87.
[24] D. Prando, A. Brenna, M.V. Diamanti, S. Beretta, F. Bolzoni, M. Ormellese, M. Pedeferri, Corrosion of Titanium: Part 1: Aggressive Environments and Main Forms of Degradation, Journal of Applied Biomaterials & Functional Materials 15(4) (2017) e291-e302.
[25] M.B. Radovanović, Z. Tasić Ž, A.T. Simonović, M.B. Petrović Mihajlović, M.M. Antonijević, Corrosion Behavior of Titanium in Simulated Body Solutions with the Addition of Biomolecules, ACS Omega 5(22) (2020) 12768-12776.
[26] A.T. Sidambe, Biocompatibility of Advanced Manufactured Titanium Implants-A Review, Materials (Basel) 7(12) (2014) 8168-8188.
[27] Z.S. Zhu, R.Y. Liu, M.G. Yan, C.X. Cao, J.L. Gu, N.P. Chen, Texture control and the anisotropy of mechanical properties in titanium sheet, Journal of Materials Science 32(19) (1997) 5163-5167.
[28] S. Gao, T. He, Q. Li, Y. Sun, Y. Sang, Y. Wu, L. Ying, Anisotropic behavior and mechanical properties of Ti-6Al-4V alloy in high temperature deformation, Journal of Materials Science 57(1) (2022) 651-670.
[29] B. Revil-Baudard, O. Cazacu, E. Massoni, Room-temperature plastic behavior and formability of a commercially pure titanium: Mechanical characterization, modeling, and validation, International Journal of Solids and Structures 228 (2021) 111121.
[30] B.S. Fromm, B.L. Adams, S. Ahmadi, M. Knezevic, Grain size and orientation distributions: Application to yielding of α-titanium, Acta Materialia 57(8) (2009) 2339-2348.
[31] S.R. Agnew, Ö. Duygulu, Plastic anisotropy and the role of non-basal slip in magnesium alloy AZ31B, International Journal of Plasticity 21(6) (2005) 1161-1193.
[32] M.H. Yoo, Slip, twinning, and fracture in hexagonal close-packed metals, Metallurgical Transactions A 12(3) (1981) 409-418.

[33] Y.B. Chun, S.H. Yu, S.L. Semiatin, S.K. Hwang, Effect of deformation twinning on microstructure and texture evolution during cold rolling of CP-titanium, Materials Science and Engineering: A 398(1) (2005) 209-219.
[34] M. Knezevic, R.A. Lebensohn, O. Cazacu, B. Revil-Baudard, G. Proust, S.C. Vogel, M.E. Nixon, Modeling bending of α-titanium with embedded polycrystal plasticity in implicit finite elements, Materials Science and Engineering: A 564(0) (2013) 116-126.
[35] G. Yoganjaneyulu, C. Sathiya Narayanan, R. Narayanasamy, Investigation on the fracture behavior of titanium grade 2 sheets by using the single point incremental forming process, Journal of Manufacturing Processes 35 (2018) 197-204.
[36] D. Ao, J. Gao, X. Chu, S. Lin, J. Lin, Formability and deformation mechanism of Ti-6Al-4V sheet under electropulsing assisted incremental forming, International Journal of Solids and Structures 202 (2020) 357-367.
[37] H. Li, S.F. Chen, S.H. Zhang, Y. Xu, H.W. Song, Deformation Characteristics, Formability and Springback Control of Titanium Alloy Sheet at Room Temperature: A Review, Materials (Basel) 15(16) (2022).
[38] T. Maeno, M. Tomobe, K.-i. Mori, Y. Ikeda, Hot stamping of titanium alloy sheets using partial contact heating, Procedia Manufacturing 15 (2018) 1149-1155.
[39] W.C. Emmens, A.H. van den Boogaard, Incremental forming by continuous bending under tension—An experimental investigation, Journal of Materials Processing Technology 209(14) (2009) 5456-5463.
[40] N. Matukhno, N. Kljestan, S.C. Vogel, M. Knezevic, Cyclic bending under tension of alloy AZ31 sheets: Influence on elongation-to-fracture and strength, Materials Science and Engineering: A 857 (2022) 144127.
[41] T.J. Roemer, T.J. Barrett, M. Knezevic, B.L. Kinsey, Y.P. Korkolis, Experimental study of continuous-bending-under-tension of AA6022-T4, Journal of Materials Processing Technology 266 (2019) 707-714.
[42] C.M. Poulin, Y.P. Korkolis, B.L. Kinsey, M. Knezevic, Over five-times improved elongation-to-fracture of dual-phase 1180 steel by continuous-bending-under-tension, Mater. Des. 161 (2019) 95-105.
[43] T.J. Barrett, S. Takagi, N. Islam, T. Kuwabara, T. Hassan, B.L. Kinsey, M. Knezevic, Y.P. Korkolis, Material modeling and simulation of continuous-bending-under-tension of AA6022-T4, Journal of Materials Processing Technology 287 (2021) 116658.
[44] M. Zecevic, M. Knezevic, Origins of improved elongation to fracture in cyclic bending under tension of AA6022-T4 sheets as revealed using crystal plasticity modeling, Mechanics of Materials 177 (2023) 104546.
[45] R. Sharma, C.M. Poulin, M. Knezevic, M.P. Miles, D.T. Fullwood, Micromechanical origins of remarkable elongation-to-fracture in AHSS TRIP steels via continuous bending under tension, Materials Science and Engineering: A 825 (2021) 141876.
[46] A. Needleman, V. Tvergaard, A numerical study of void distribution effects on dynamic, ductile crack growth, Engineering Fracture Mechanics 38(2) (1991) 157-173.
[47] A. Needleman, V. Tvergaard, Dynamic crack growth in a nonlocal progressively cavitating solid, European Journal of Mechanics - A/Solids 17(3) (1998) 421-438.
[48] X. Li, M. Xu, Z. Zhang, Hot damage evolution in a high strength aluminum alloy during hot forming: a study using the Gurson–Tvergaard–Needleman model, Journal of Materials Research and Technology 14 (2021) 1366-1376.

[49] H. Wu, X. Zhuang, Z. Zhao, Extended GTN model for predicting ductile fracture under a broad range of stress states, International Journal of Solids and Structures 239-240 (2022) 111452.
[50] H. Gholipour, F.R. Biglari, K. Nikbin, Experimental and numerical investigation of ductile fracture using GTN damage model on in-situ tensile tests, International Journal of Mechanical Sciences 164 (2019) 105170.
[51] N. Pitkin, P. Noell, D.T. Fullwood, M. Knezevic, Damage evolution and ductile fracture of commercially-pure titanium sheets subjected to simple tension and cyclic bending under tension, Journal of Materials Research and Technology 32 (2024) 124-139.
[52] N. Miller, N. Pitkin, T.M.T. Oishi, D. Mensah, M. Knezevic, M. Miles, D. Fullwood, Multiscale characterization of dislocation development during cyclic bending under tension in commercially pure titanium, Journal of Materials Research and Technology 32 (2024) 2513-2527.
[53] T.M.T. Oishi, N. Pitkin, N. Miller, D. Mensah, D.T. Fullwood, M.P. Miles, B.L. Kinsey, M. Knezevic, Influence of specimen width on the elongation-to-fracture in cyclic-bending-under-tension of commercially pure titanium sheets, International Journal of Mechanical Sciences 278 (2024) 109447.
[54] Z. Cai, X. Cheng, J. Chen, T. Xiang, G. Xie, Optimized mechanical properties of titanium-oxygen alloys by powder metallurgy, Journal of Materials Research and Technology 21 (2022) 4151-4163.
[55] X. Shi, X. Wang, B. Chen, J. Umeda, A. Bahador, K. Kondoh, J. Shen, Precision control of oxygen content in CP-Ti for ultra-high strength through titanium oxide decomposition: An in-situ study, Materials & Design 227 (2023) 111797.
[56] Y. Chong, M. Poschmann, R. Zhang, S. Zhao, M.S. Hooshmand, E. Rothchild, D.L. Olmsted, J.W. Morris, Jr., D.C. Chrzan, M. Asta, A.M. Minor, Mechanistic basis of oxygen sensitivity in titanium, Sci Adv 6(43) (2020).
[57] Z. Liu, G. Welsch, Effects of oxygen and heat treatment on the mechanical properties of alpha and beta titanium alloys, Metallurgical Transactions A 19(3) (1988) 527-542.
[58] Z. Cai, T. Xiang, W. Bao, J. Chen, T. Gao, G. Xie, Enhancing strength and ductility of pure titanium by interstitial oxygen atoms, Materials Science and Engineering: A 854 (2022) 143806.
[59] K. Weinberg, Void nucleation by vacancy condensation, PAMM 8(1) (2008) 10249-10250.
[60] P.J. Noell, J.E.C. Sabisch, D.L. Medlin, B.L. Boyce, Nanoscale conditions for ductile void nucleation in copper: Vacancy condensation and the growth-limited microstructural state, Acta Materialia 184 (2020) 211-224.
[61] S.-M. Lee, Effects of Impurities on Stress Induced Void Formation in Al-1%Si Conductors, Transactions on Electrical and Electronic Materials 2(3) (2001).
[62] W. Wciślik, S. Lipiec, Voids Development in Metals: Numerical Modelling, Materials (Basel) 16(14) (2023).
[63] W. Wciślik, S. Lipiec, Void-Induced Ductile Fracture of Metals: Experimental Observations, Materials (Basel) 15(18) (2022).
[64] W. Wciślik, R. Pała, Some Microstructural Aspects of Ductile Fracture of Metals, Materials (Basel) 14(15) (2021).
[65] M.J. Nemcko, D.S. Wilkinson, On the damage and fracture of commercially pure magnesium using x-ray microtomography, Materials Science and Engineering: A 676 (2016) 146-155.

[66] M.J. Nemcko, D.S. Wilkinson, Impact of microstructure on void growth and linkage in pure magnesium, International Journal of Fracture 200(1) (2016) 31-47.
[67] T.R. Bieler, M.A. Crimp, Y. Yang, L. Wang, P. Eisenlohr, D.E. Mason, W. Liu, G.E. Ice, Strain heterogeneity and damage nucleation at grain boundaries during monotonic deformation in commercial purity titanium, JOM 61(12) (2009) 45-52.
[68] T. LaGrange, Influence of grain boundary character on void formation in nanotwinned copper, European Microscopy Congress 2016: Proceedings2016, pp. 217-218.
[69] U.B. Asim, M.A. Siddiq, M.E. Kartal, A CPFEM based study to understand the void growth in high strength dual-phase titanium alloy (Ti-10V-2Fe-3Al), International Journal of Plasticity 122 (2019) 188-211.
[70] G. Avramovic-Cingara, C.A.R. Saleh, M.K. Jain, D.S. Wilkinson, Void Nucleation and Growth in Dual-Phase Steel 600 during Uniaxial Tensile Testing, Metallurgical and Materials Transactions A 40(13) (2009) 3117-3127.
[71] P. Noell, J. Carroll, K. Hattar, B. Clark, B. Boyce, Do voids nucleate at grain boundaries during ductile rupture?, Acta Materialia 137 (2017) 103-114.
[72] P.J. Noell, R.B. Sills, B.L. Boyce, Suppression of Void Nucleation in High-Purity Aluminum via Dynamic Recrystallization, Metallurgical and Materials Transactions A 51(1) (2020) 154-166.
[73] I. Barsoum, J. Faleskog, Rupture mechanisms in combined tension and shear—Experiments, International Journal of Solids and Structures 44(6) (2007) 1768-1786.
[74] I. Barsoum, J. Faleskog, Rupture mechanisms in combined tension and shear—Micromechanics, International Journal of Solids and Structures 44(17) (2007) 5481-5498.
[75] C.D. Beachem, G.R. Yoder, Elastic-plastic fracture by homogeneous microvoid coalescence tearing along alternating shear planes, Metallurgical Transactions 4(4) (1973) 1145-1153.
[76] W.M. Garrison, N.R. Moody, Ductile fracture, Journal of Physics and Chemistry of Solids 48(11) (1987) 1035-1074.
[77] M.F. Horstemeyer, J. Lathrop, A.M. Gokhale, M. Dighe, Modeling stress state dependent damage evolution in a cast Al–Si–Mg aluminum alloy, Theoretical and Applied Fracture Mechanics 33(1) (2000) 31-47.
[78] M.F. Horstemeyer, A.M. Gokhale, A void–crack nucleation model for ductile metals, International Journal of Solids and Structures 36(33) (1999) 5029-5055.
[79] N. Pathak, J. Adrien, C. Butcher, E. Maire, M. Worswick, Experimental stress state-dependent void nucleation behavior for advanced high strength steels, International Journal of Mechanical Sciences 179 (2020) 105661.
[80] J. Samei, D.E. Green, J. Cheng, M.S. de Carvalho Lima, Influence of strain path on nucleation and growth of voids in dual phase steel sheets, Materials & Design 92 (2016) 1028-1037.
[81] T.B. Cox, J.R. Low, An investigation of the plastic fracture of AISI 4340 and 18 Nickel-200 grade maraging steels, Metallurgical transactions 5(6) (1974) 1457-1470.
[82] J.R. Fisher, J. Gurland, Void nucleation in spheroidized carbon steels Part 1: Experimental, Metal Science 15(5) (1981) 185-192.
[83] J.L. Maloney, W.M. Garrison, Comparison of void nucleation and growth at MnS and Ti2CS inclusions in HY180 steel, Scripta Metallurgica 23(12) (1989) 2097-2100.
[84] J. Sun, Effect of stress triaxiality on micro-mechanisms of void coalesence and micro-fracture ductility of materials, Engineering Fracture Mechanics 39(5) (1991) 799-805.

[85] G. Testa, N. Bonora, A. Ruggiero, G. Iannitti, D. Gentile, Stress triaxiality effect on void nucleation in ductile metals, Fatigue & Fracture of Engineering Materials & Structures 43(7) (2020) 1473-1486.
[86] S. Xu, X. Deng, Nanoscale void nucleation and growth and crack tip stress evolution ahead of a growing crack in a single crystal, Nanotechnology 19(11) (2008) 115705.
[87] N. Matukhno, N. Kljestan, M. Knezevic, Enhancing elongation and trading off strength versus ductility of commercially pure titanium sheets using cyclic bending under tension and annealing, International Journal of Solids and Structures 276 (2023) 112324.
[88] Dislocation mobility, in: J.J. Gilman (Ed.), Electronic Basis of the Strength of Materials, Cambridge University Press, Cambridge, 2003, pp. 201-246.
[89] J.J. Gilman, The Plastic Resistance of Crystals, Australian Journal of Physics 13(2) (1960) 327-346.
[90] E. Nadgornyi, Dislocation dynamics and mechanical properties of crystals, Progress in Materials Science 31 (1988) 1-530.
[91] S. Zhang, J. Zhou, L. Wang, H. Liu, S. Dong, Crack nucleation due to dislocation pile-ups at twin boundary–grain boundary intersections, Materials Science and Engineering: A 632 (2015) 78-81.
[92] Z. Shen, R.H. Wagoner, W.A.T. Clark, Dislocation and grain boundary interactions in metals, Acta Metallurgica 36(12) (1988) 3231-3242.
[93] X. Li, X. Jiang, Effects of dislocation pile-up and nanocracks on the main crack propagation in crystalline metals under uniaxial tensile load, Engineering Fracture Mechanics 212 (2019) 258-268.
[94] R. Sandström, Formation of Cells and Subgrains and Its Influence on Properties, Metals, 2022.
[95] Q. Liu, N. Hansen, Geometrically necessary boundaries and incidental dislocation boundaries formed during cold deformation, Scripta Metallurgica et Materialia 32(8) (1995) 1289-1295.
[96] P. Yang, P. Zhao, Void nucleation at dislocation boundaries aided by the synergy of multiple dislocation pile-ups, International Journal of Plasticity 171 (2023) 103779.
[97] D.A. Hughes, N. Hansen, Microstructural evolution in nickel during rolling from intermediate to large strains, MTA 24(9) (1993) 2022-2037.
[98] Q. Yu, L. Qi, T. Tsuru, R. Traylor, D. Rugg, J.W. Morris, M. Asta, D.C. Chrzan, A.M. Minor, Origin of dramatic oxygen solute strengthening effect in titanium, Science 347(6222) (2015) 635-639.
[99] X. He, M. Wang, C. Hu, L. Xu, Study of the relationship among total oxygen, inclusions and fatigue properties of gear steel, Materials Science and Engineering: A 827 (2021) 141999.
[100] C.-B. Shi, X.-C. Chen, H.-J. Guo, Z.-J. Zhu, H. Ren, Assessment of Oxygen Control and Its Effect on Inclusion Characteristics during Electroslag Remelting of Die Steel, steel research international 83(5) (2012) 472-486.
[101] J.S. Seo, C. Lee, H.J. Kim, Influence of Oxygen Content on Microstructure and Inclusion Characteristics of Bainitic Weld Metals, ISIJ International 53(2) (2013) 279-285.
[102] A.S. Argon, J. Im, Separation of second phase particles in spheroidized 1045 steel, Cu-0.6pct Cr alloy, and maraging steel in plastic straining, Metallurgical Transactions A 6(4) (1975) 839-851.

[103] C.M. Laursen, S.A. DeJong, S.M. Dickens, A.N. Exil, D.F. Susan, J.D. Carroll, Relationship between ductility and the porosity of additively manufactured AlSi10Mg, Materials Science and Engineering: A 795 (2020) 139922.
[104] N.D. Vallejo, N. Kljestan, N. Ayers, M. Knezevic, Y. Sohn, Flaw type dependent tensile properties of 316L stainless steel additively manufactured by laser powder bed fusion, Results in Materials 15 (2022) 100315.
[105] A.E. Wilson-Heid, A.M. Beese, Combined effects of porosity and stress state on the failure behavior of laser powder bed fusion stainless steel 316L, Additive Manufacturing 39 (2021) 101862.
[106] R.A. Hardin, C. Beckermann, Effect of Porosity on Deformation, Damage, and Fracture of Cast Steel, Metallurgical and Materials Transactions A 44(12) (2013) 5316-5332.
[107] R.A. Hardin, C. Beckermann, Effect of Porosity on the Stiffness of Cast Steel, Metallurgical and Materials Transactions A 38(12) (2007) 2992-3006.
[108] R.A. Hardin, C. Beckermann, Prediction of the Fatigue Life of Cast Steel Containing Shrinkage Porosity, Metallurgical and Materials Transactions A 40(3) (2009) 581-597.
[109] M. Griffiths, Effect of Neutron Irradiation on the Mechanical Properties, Swelling and Creep of Austenitic Stainless Steels, Materials (Basel) 14(10) (2021).
[110] T. Davis, D. Healy, A. Bubeck, R. Walker, Stress concentrations around voids in three dimensions: The roots of failure, Journal of Structural Geology 102 (2017) 193-207.
[111] H. Conrad, Effect of interstitial solutes on the strength and ductility of titanium, Progress in Materials Science 26(2) (1981) 123-403.
[112] Y. Murayama, M. Mikami, S. Ishiyama, S. Hanada, Effect of Oxygen on Deformation Behavior of Texture Controlled Titanium, Journal of the Japan Institute of Metals 57(6) (1993) 628-636.
[113] J. Wang, X. Zhang, Twinning effects on strength and plasticity of metallic materials, MRS Bulletin 41(4) (2016) 274-281.
[114] J. Wang, N. Tao, Deformation Twinning Induced High Tensile Ductility of a Gradient Nanograined Cu-Based Alloy, Nanomaterials (Basel) 11(9) (2021).
[115] M.R. Barnett, Twinning and the ductility of magnesium alloys: Part I: “Tension” twins, Materials Science and Engineering: A 464(1) (2007) 1-7.